CMS Physics Analysis Summary

Contact: cms-pag-conveners-higgs@cern.ch 2016/08/04

Updated measurements of Higgs boson production in the diphoton decay channel at $\sqrt{s} = 13$ TeV in pp collisions at CMS.

The CMS Collaboration

Abstract

An observation of the Higgs boson production for the two photon decay channel with the 2016 LHC Run 2 data is described. The analysis is performed using the dataset recorded by the CMS experiment at the LHC from pp collisions at centre-of-mass energy of 13 TeV corresponding to an integrated luminosity of 12.9 fb^{-1}. The observed significance for the standard model Higgs boson at the Run 1 ATLAS+CMS combined $m_H = 125.09$ GeV is 5.6 σ, where 6.2 σ is expected. A maximum significance of 6.1 σ is observed at 126.0 GeV. The best-fit signal strength relative to the standard model prediction is $0.95 \pm 0.20 = 0.95 \pm 0.17$ (stat.) $^{+0.10}_{-0.07}$ (syst.) $^{+0.08}_{-0.05}$ (theo.) when the mass parameter is profiled in the fit, and $0.91 \pm 0.20 = 0.91 \pm 0.17$ (stat.) $^{+0.09}_{-0.07}$ (syst.) $^{+0.08}_{-0.05}$ (theo.) when it is fixed to $m_H = 125.09$ GeV. The fiducial cross section is measured to be $\hat{\sigma}_{fid} = 69^{+18}_{-22}$ fb $= 69^{+16}_{-22}(\text{stat.})^{+8}_{-6}(\text{syst.})$ fb, where the standard model theoretical prediction is 73.8 ± 3.8 fb.

1 Introduction

The standard model of particle physics (SM) has been very successful in explaining high-energy experimental data [1–3]. During the Run 1 period of the CERN LHC, a new particle was discovered by both ATLAS [4] and CMS [5] experiments. The collected experimental evidence is consistent with the particle being the Higgs boson, the quantum of the scalar field postulated by the Higgs mechanism [6–8].

The discovery was followed by a comprehensive set of studies of the Higgs boson decay channels and production modes accessible with the full LHC Run 1 dataset. The CMS experiment's most sensitive analysis of the Higgs boson to diphoton decay, using the full Run 1 dataset, which resulted in a standalone observation of the Higgs boson decaying to two photons, can be found in [9]. Combined measurements from ATLAS and CMS [10] showed that the properties of the new boson are fully consistent with expectations for a SM Higgs boson with mass $125.09 \pm 0.21(\text{stat.}) \pm 0.11(\text{syst.})$ GeV.

Despite the small branching ratio predicted by the SM ($\approx 0.2\%$), the $\mathrm{H} \to \gamma\gamma$ decay channel provides a clean final state with an invariant mass peak that can be reconstructed with great precision. As a consequence, $\mathrm{H} \to \gamma\gamma$ was one of the most important channels involved in the discovery and first measurements of the Higgs boson properties. In the LHC Run 2, where the centre-of-mass collision energy has increased to 13 TeV, this channel remains very sensitive and can be used for precise characterization of Higgs boson's properties.

CMS has already presented preliminary results on Higgs boson production in the diphoton decay channel with pp collisions at centre-of-mass energy of 13 TeV, based on $2.7\,\text{fb}^{-1}$ of data collected with the CMS experiment at the LHC in 2015 [11]. The analysis followed the strategy described in [9]. In this summary, the data collected by CMS in 2016 so far, corresponding to $12.9\,\text{fb}^{-1}$ of integrated luminosity of pp collisions, are used to make additional measurements, namely of the cross sections (inclusive and fiducial) and couplings of the Higgs boson.

2 The CMS detector

A detailed description of the CMS detector can be found in Ref. [12]. The central feature is a superconducting solenoid, 13 m in length and 6 m in diameter, which provides an axial magnetic field of 3.8 T. The bore of the solenoid is instrumented with particle detection systems. The steel return yoke outside the solenoid is instrumented with gas detectors used to identify muons. Charged particle trajectories are measured by the silicon pixel and strip tracker, with full azimuthal coverage within $|\eta| < 2.5$. A lead-tungstate crystal electromagnetic calorimeter (ECAL) and a brass/scintillator hadron calorimeter (HCAL) surround the tracking volume and cover the region $|\eta| < 3$. The electromagnetic calorimeter consists of 75 848 lead tungstate crystals, which provide coverage in pseudorapidity $|\eta| < 1.479$ in a barrel region (EB) and $1.479 < |\eta| < 3.0$ in two endcap regions (EE). A preshower detector consisting of two planes of silicon sensors interleaved with a total of $3X_0$ of lead is located in front of the EE. A lead/silicon-strip preshower detector is located in front of the ECAL endcap. The preshower detector includes two planes of silicon sensors measuring the x and y coordinates of the impinging particles. A steel/quartz-fibre Cherenkov forward calorimeter extends the calorimetric coverage to $|\eta| < 5.0$. In the region $|\eta| < 1.74$, the HCAL cells have widths of 0.087 in both pseudorapidity and azimuth (ϕ). In the (η, ϕ) plane, and for $|\eta| < 1.48$, the HCAL cells map on to 5×5 ECAL crystal arrays to form calorimeter towers projecting radially outwards from points slightly offset from the nominal interaction point. In the endcap, the ECAL arrays matching the HCAL cells contain fewer crystals. The calibration of the ECAL uses the azimuthal

symmetry of the energy flow in minimum-bias events, $\pi^0, \eta^0 \to \gamma\gamma$, $W \to e\nu$, and $Z \to ee$ decays. Changes in the transparency of the ECAL crystals due to irradiation during the LHC running periods and their subsequent recovery is monitored continuously and corrected for, using light injected from a laser system. In the barrel section of the ECAL, an energy resolution of about 1% is achieved for unconverted or late-converting photons in the tens of GeV energy range. The remaining barrel photons have a resolution of about 1.3% up to a pseudorapidity of $|\eta| = 1$, rising to about 2.5% at $|\eta| = 1.4$. In the endcaps, the resolution of unconverted or late-converting photons is about 2.5%, while the remaining endcap photons have a resolution between 3 and 4% [13].

3 Data samples and reconstruction

The data sample used in the analysis corresponds to an integrated luminosity of $12.9\,\text{fb}^{-1}$, recorded at the LHC in pp collisions at a centre-of-mass energy of 13 TeV in 2016.

Simulated signal events are generated using MADGRAPH5_aMC@NLO at next-to-leading order (NLO) [14] in perturbative quantum chromodynamics (QCD), the parton level samples being interfaced to PYTHIA8 [15] for parton showering and hadronization. For some samples, the precision of the calculation is beyond NLO as processes with different jet multiplicities at NLO are merged using the FxFx scheme [16]. The CUETP8M1 PYTHIA tune parameter set is used [17]. The signal cross-sections and branching ratios recommended by the LHC Higgs cross-section working group are used [18].

The dominant background to $H \to \gamma\gamma$ consists of the irreducible prompt diphoton production, and the reducible backgrounds from $\gamma +$ jet and QCD multijet, where the jets are misidentified as isolated photons. Background events, used for the trainings of multivariate discriminants and for category optimization, have been simulated using various generators. The diphoton prompt-prompt background is modeled with the Sherpa [19] generator. It includes the born processes with up to 3 additional jets as well as the box processes at leading order (LO). Prompt-fake and fake-fake backgrounds are modeled with PYTHIA8. A filter was applied to the multijet and $\gamma +$ jet samples in order to enhance the production of jets with a large fraction of electromagnetic energy. This filter requires a potential photon signal (electromagnetic activity) coming from photons, electrons, or neutral hadrons, with $p_T > 15$ GeV. The $W\gamma$, $Z\gamma$ and Drell–Yan events are simulated with MADGRAPH5_aMC@NLO using the following specifications:

- $W\gamma$ samples are generated at leading order with the MLM merging scheme with up to 3 jets from the matrix element,
- $Z\gamma$ samples are generated at leading order with the FxFx merging scheme with 1 jet from the matrix element,
- Drell-Yann samples used for jet studies are generated at next-to-leading order using the FxFx merging scheme, with 2 up to jets from the matrix element.

The detailed response of the CMS detector is simulated based on the GEANT 4 [20] package. The simulation includes overlapping pp interactions in the nominal bunch (pileup) as well as in the previous 12 and subsequent 4 bunch-crossings (out-of-time pileup). Simulated events are generated with a Poissonian pileup distribution. They are then reweighed to match the distribution of the number of interactions per event measured from data in the full dataset. The average number of pileup interactions measured in data amounts to 18.5.

Diphoton triggers with asymmetric transverse energy (E_T) thresholds are used. The trigger

used on the 2016 data has slightly looser requirements than the trigger used for the 2015 data, detailed in [11]. These changes occurred alongside improvements to the reconstruction of electrons and photons within the trigger system. The trigger selection requires:

- a loose identification using cluster shower shapes,
- a loose isolation requirement and a selection on the ratio of the energy of the photon candidates in the HCAL and the ECAL (H/E).

The energy sum of 3×3 crystals centered on the most energetic crystal in the candidate electromagnetic-magnetic cluster divided by the energy of the candidate (the R_9 variable) is used to identify photons undergoing a conversion in the tracker material up to the ECAL surface.

The identification of the Higgs boson interaction vertex uses tracks recoiling from the diphoton system and any tracks from photons which have undergone conversion. In this case, conversions are reconstructed from a combination of tracks of charged particles. Such tracks are required to be of opposite curvature (representing opposite-signed charged particles) and be parallel near the candidate conversion vertex.

All candidate particles are reconstructed using the particle-flow algorithm (PF) [21], which relies on the information from all CMS sub-detectors to reconstruct different types of particles produced in the event. Photons are made of clusters of energy deposited in the ECAL. The cluster reconstruction recovers the energy of photons that convert due to the material in front of the ECAL. The algorithm consists of three steps. First, cluster seeds are identified as local energy maxima above a given threshold. Second, topological clusters are grown from the seeds by aggregating crystals with at least one side in common with a clustered crystal, and with an energy in excess of a given threshold. These thresholds represent about two standard deviations of the electronic noise in the ECAL (i.e. 80 MeV in the barrel and up to 300 MeV in the endcaps depending on $|\eta|$). Finally the clusters are merged into "superclusters", the position of which is given as the energy-weighted average position of all the energy deposits within it. The main purpose of this step is to recover the energy lost due to bremsstrahlung by electrons and positrons emerging from converted photons. This clustering also allows pileup to be mitigated.

The photon energy is computed starting from the bare sum of the calibrated energy of ECAL reconstructed hits. The preshower energy is also added for superclusters in the region covered by this detector ($1.65 < |\eta| < 2.6$). Two layers of corrections are used. The first consists of crystal-level corrections necessary to equalize the channel-to-channel response variations. The second corrects for the containment of the shower in the clustered crystals, and the energy losses of photons which convert in material upstream of the calorimeter. These corrections are computed using a multivariate regression BDT, as described in [13]. This technique is able to predict simultaneously the energy of the photon and its median uncertainty. The regression is trained on simulated events to correct to the true photon energy. The variables used in the regression are shower shape and position variables, preshower information, and global event observables sensitive to pileup.

An additional photon energy scale correction is derived from the detailed comparison of the mass distribution of $Z \to e^+e^-$ events in data and simulation. Conjointly, an additional smearing that needs to be applied to the reconstructed photon energy in the simulation to match the resolution in data is derived from this comparison. These residual corrections are computed for photons into four η regions (two in the barrel and two in the endcaps) and two categories of R_9. The uncertainties on the measurements of the photon scale and resolution are included in the systematic uncertainties. Fig. 1 shows the comparison of data and simulation for the Z invariant mass distributions in four η, R_9 categories after all the energy corrections described

above.

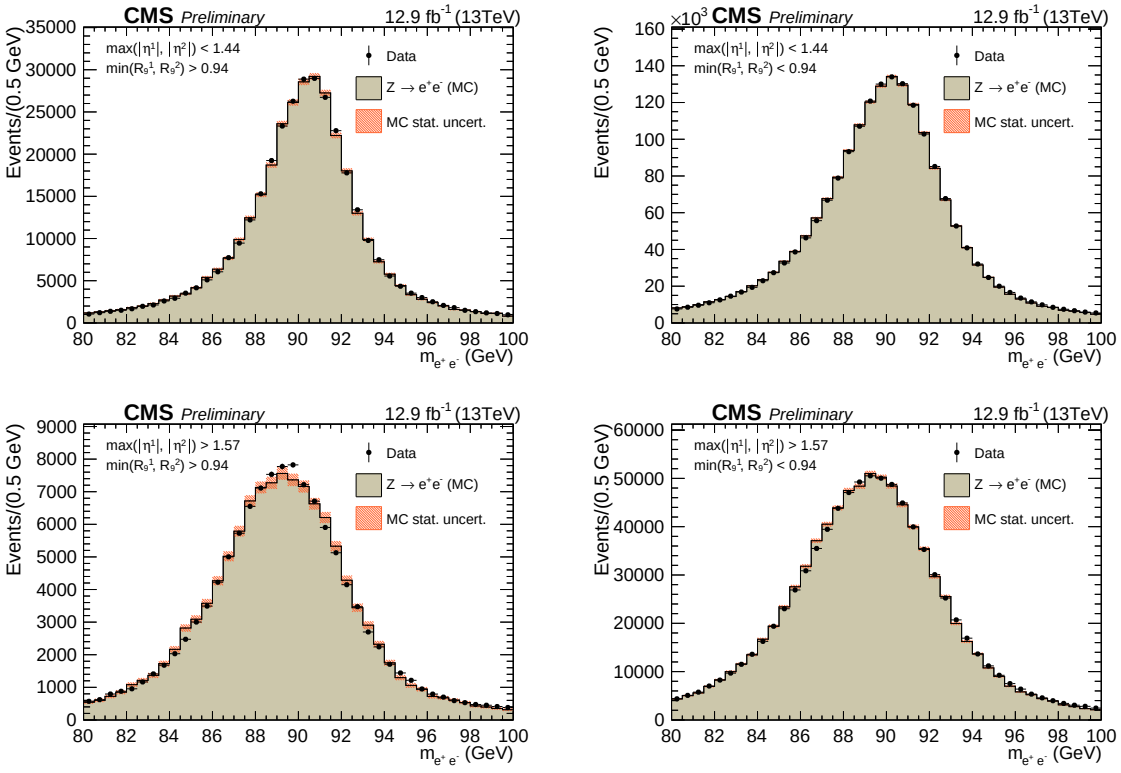

Figure 1: Comparison of the dielectron invariant mass distributions in data and simulation for $Z \to e^+e^-$ events where electrons are reconstructed as photons. The events are split into categories according to the η and R_9 of the electrons. The simulated distribution is normalized to the integral of the data distribution in the range 87 GeV$< m_{e^+e^-} <$ 93 GeV.

In order to improve the level of agreement, the variables with substantial disagreement between data and simulation are corrected using a scale factor derived from a sample of electrons reconstructed as photons and selected with the tag and probe method in $Z \to e^+e^-$ events. The variables affected by this correction are R_9, η-width (the supercluster width in the η direction) and S_4 (the energy ratio of 2x2 and 5x5 array of crystals centred on the seed crystal). The correction is applied separately in the ECAL barrel and endcaps. A specific systematic, described in Section 10 is included as a result of introducing this correction.

The tracks of charged particles reconstructed in the central tracker and the energy deposits reconstructed in the calorimeters are clustered into jets with the anti-k_T algorithm [22] using a value of 0.4 for the distance parameter R, implemented in the FastJet package [23]. Charged candidates associated with a vertex other than the selected vertex for the event are excluded. Jets are required to have transverse momentum p_T at least 20 GeV and $|\eta| < 4.7$. For jets with $|\eta| > 2.5$, outside the tracker acceptance, a pileup mitigation technique exploiting the width of the jet is used. The width of the jet, defined as $< R^2 >= \frac{\sum_{constituents} p_T^2 \Delta R^2}{\sum_{constituents} p_T^2}$, where $\Delta R = \sqrt{(\Delta\eta)^2 + (\Delta\phi)^2}$ is between the constituent and the jet axis, is required to be less than 0.03.

The jet energy measurement is corrected for detector effects using samples of dijet, γ + jet, and Z + jet events [24]. An event-by-event jet-area-based correction [23–25] is applied to remove the energy from additional collisions in the same bunch crossing (pileup).

4 Vertex location

The determination of the primary vertex associated with the Higgs boson has a direct impact on the diphoton mass resolution. If the interaction point is known to better than about 1 cm, the resolution is dominated by the ECAL energy contribution only. If the interaction point is incorrectly assigned, the resolution worsens substantially because of the effect on the calculation of the opening angle between the photons, and thus the invariant mass.

The diphoton vertex assignment relies on a Boosted Decision Tree (BDT), labelled here as $\mathrm{BDT_{VTX\,ID}}$. The inputs to $\mathrm{BDT_{VTX\,ID}}$ are observables related to tracks recoiling against the diphoton system: $\sum_i |\vec{p}^{\,i}_T|^2$, -$\sum_i (\vec{p}^{\,i}_T \cdot \frac{\vec{p}^{\,\gamma\gamma}_T}{|\vec{p}^{\,\gamma\gamma}_T|})$ and $(|\sum_i \vec{p}^{\,i}_T| - p_{\mathrm{T}}^{\gamma\gamma})/(|\sum_i \vec{p}^{\,i}_T| + p_{\mathrm{T}}^{\gamma\gamma})$ where $\vec{p}^{\,i}_T$ is the transverse momentum of the *i-th* track associated with a given vertex and $\vec{p}^{\,\gamma\gamma}_T$ is the transverse momentum of the diphoton system. The sum runs over all charged particle flow candidates associated to the given vertex. In the presence of tracks from photons converted in the tracker material, two additional variables are used as input to $\mathrm{BDT_{VTX\,ID}}$: the number of conversions and the pull $|z_{\mathrm{vtx}} - z_{\mathrm{e}}|/\sigma_z$ between the longitudinal position of the reconstructed vertex, z_{vtx}, and the longitudinal position of the vertex estimated using conversion track(s), z_{e}. The variable σ_z here denotes the uncertainty on z_{e}.

A second vertex-related multivariate discriminant is designed to estimate, event-by-event, the probability for the vertex assignment to be within 1 cm of the diphoton interaction point. It is hereafter labelled as $\mathrm{BDT_{VTX\,PROB}}$. This is used in conjunction with the event-by-event estimate of the photon energy resolution to estimate the diphoton mass resolution using a BDT (see Section 6). $\mathrm{BDT_{VTX\,PROB}}$ is trained using simulated $\mathrm{H} \to \gamma\gamma$ events using the following input variables:

- the number of vertices in each event,
- the values of the $\mathrm{BDT_{VTX\,ID}}$ output for the three most likely vertices in each event,
- the distances between the chosen vertex and the second and third choices,
- the transverse momentum of the diphoton system ($p_{\mathrm{T}}^{\gamma\gamma}$),
- the number of photons with an associated conversion track.

The per-event probability to choose the vertex within 1 cm of the true one is parametrized as a function of the $\mathrm{BDT_{VTX\,PROB}}$ output with a 4^{th} order polynomial separately for converted and unconverted photons.

The performance of the $\mathrm{H} \to \gamma\gamma$ vertex identification algorithm is validated using $\mathrm{Z} \to \mu^+\mu^-$ events where the vertices are refitted ignoring the muon tracks to mimic a diphoton system. In addition, the use of tracks from converted photons to locate the vertex is validated using γ + jet events. The agreement between data and simulation shows a discrepancy in the distribution of the location of primary vertices. In particular, the width of the distribution in data was measured to be of the order of 3.6 cm, while in simulation this quantity was generated with a value of 5.14 cm. In order to resolve this, events where the selected vertex is more than 0.1 cm away from the generated vertex were re-weighted such that the distribution of location of primary vertices had a width of 3.6 cm.

The efficiency of choosing the vertex within 1 cm of the true vertex in $\mathrm{H} \to \gamma\gamma$ simulated events is shown in Fig. 2 as a function of the p_{T} of the diphoton pair and in Fig. 3 as a function of the number of primary vertices in the event. The efficiency of finding the correct vertex integrated over the entire Higgs boson p_{T} spectrum is about 80%.

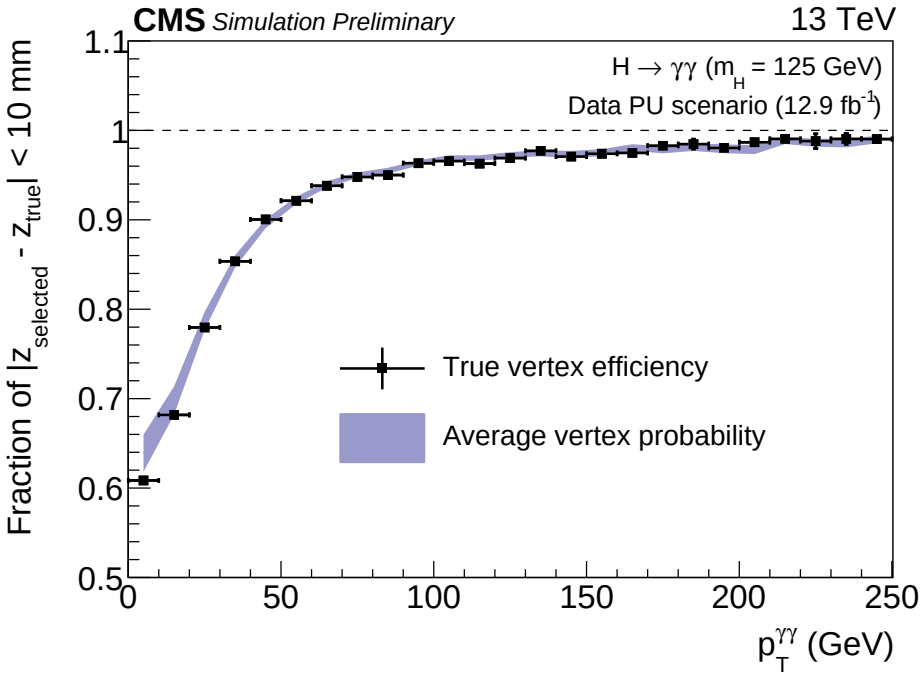

Figure 2: Comparison of the true vertex identification efficiency and the average estimated vertex probability as a function of the reconstructed diphoton p_{T} in simulated $\mathrm{H} \to \gamma\gamma$ events with $m_{\mathrm{H}} = 125$ GeV. Events are weighted according to the cross-sections of the different production modes and to match distributions of pileup and location of primary vertices in data.

5 Photon Selection

The event selection requires two photon candidates with $p_{\mathrm{T}}^{\gamma 1} > m_{\gamma\gamma}/3$ and $p_{\mathrm{T}}^{\gamma 2} > m_{\gamma\gamma}/4$. The use of p_{T} thresholds scaled by $m_{\gamma\gamma}$ prevents the distortion of the low end of the $m_{\gamma\gamma}$ spectrum. Both photons must also satisfy the pseudo-rapidity requirement $|\eta| < 2.5$, excluding the barrel-endcap transition region $1.44 < |\eta| < 1.57$. The excluded region removes from the acceptance the last two rings of crystals in the barrel, to ensure complete containment of accepted showers, and the first ring of trigger towers in the endcap which is obscured by cables and services exiting between the barrel and endcap. The geometrical acceptance requirement is applied to the supercluster position in the ECAL, and the p_{T} threshold is applied after the vertex assignment.

The photon identification is applied after a preselection using a multivariate approach ($\mathrm{BDT}_{\gamma\,\mathrm{ID}}$), to distinguish prompt photons from non-prompt photon background. The preselection requires all diphoton candidates to satisfy criteria more stringent than the trigger. First, the largest-p_{T} photon (leading) is required to have $p_{\mathrm{T}} > 30$ GeV and the second largest (subleading) to have $p_{\mathrm{T}} > 20$ GeV. Both have to satisfy an electron veto which removes the photon candidate if its supercluster is matched to an electron track with no missing hits in the innermost tracker layers.

Additionally the following observables are used in the preselection:

1. $\sigma_{\eta\eta}$: the energy-weighted standard deviation of single cluster η within a 5x5 array of crystals centered on the crystal with maximum energy;
2. H/E: the energy collected by the HCAL towers within a cone of radius 0.15 centred on the supercluster position, divided by the supercluster energy;

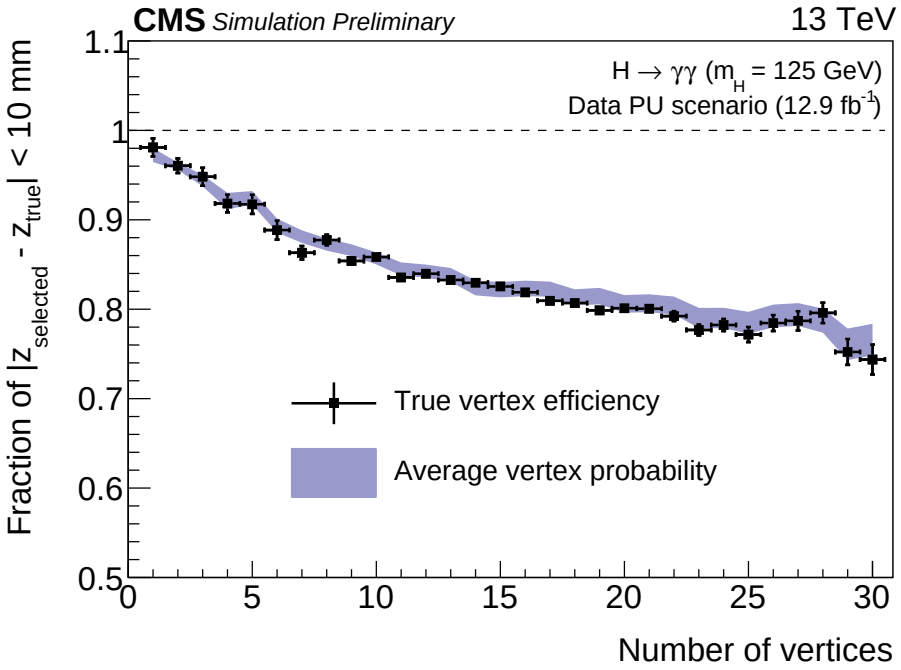

Figure 3: Comparison of the true vertex identification efficiency and the average estimated vertex probability as a function of the number of primary vertices in simulated $H \to \gamma\gamma$ events with $m_H = 125$ GeV. Events are weighted according to the cross-sections of the different production modes and to match distributions of pileup and location of primary vertices in data.

3. photon isolation: the transverse energy sum of all particles identified as photons falling inside a cone of radius 0.3 around the photon candidate direction. The sum is corrected for the contribution of the pileup estimated from the product of the measured energy density ρ for the event, where ρ is the median pileup estimator implemented in FASTJET [23], and an effective area roughly corresponding to the isolation cone;

4. tracker isolation in a hollow cone: the transverse momentum sum of all tracks falling in a cone of radius 0.3 around the photon candidate direction, excluding tracks falling in an inner cone of radius 0.04;

5. R_9;

6. charged hadron isolation: the sum of transverse momenta of charged particles inside a cone of radius 0.3 around the photon candidate. A selection on this variable is introduced to mimic the selection applied when processing photon candidates before they enter the flow of the analysis.

In addition to the requirements reported in Table 1 both photons must satisfy either $R_9 > 0.8$, charged hadron isolation < 20 GeV or charged hadron isolation relative to $p_T < 0.3$.

The $\text{BDT}_{\gamma\,\text{ID}}$ is trained using simulated $\gamma +$ jet events where the prompt photons are used as the signal and the non-prompt photons as the background, and both are required to pass the preselection. The $\text{BDT}_{\gamma\,\text{ID}}$ is using the following inputs:

- shower shape observables;

	H/E	$\sigma_{\eta\eta}$	R_9	photon iso.	tracker iso.
ECAL barrel; $R_9 > 0.85$	<0.08	–	>0.5	–	–
ECAL barrel; $R_9 \leq 0.85$	<0.08	<0.015	>0.5	< 4.0	< 6.0
ECAL endcaps; $R_9 > 0.90$	<0.08	–	>0.8	–	–
ECAL endcaps; $R_9 \leq 0.90$	<0.08	<0.035	>0.8	< 4.0	< 6.0

Table 1: Preselection requirements

- isolation variables using the sum of transverse energy of photons (photon isolation), and of charged hadrons (charged hardon isolation) falling in a cone of radius 0.3 around the candidate photon direction. Two charged hadron isolations are used, respectively considering hadrons coming from the chosen vertex and the vertex which yields the largest isolation sum. The latter is effective in rejecting photon candidates originating from mis-identification of jets from a vertex other than the chosen one;
- the median energy density per unit area in the event, ρ, in order for the $\mathrm{BDT}_{\gamma\,\mathrm{ID}}$ to be independent of pileup;
- photon kinematic observables (pseudorapidity and energy), allowing the $\mathrm{BDT}_{\gamma\,\mathrm{ID}}$ to account for the dependence of the shower topology and isolation variables on η and p_{T}.

Fig. 4 (a) shows the $\mathrm{BDT}_{\gamma\,\mathrm{ID}}$ score of the lowest-scoring photon from all diphoton pairs with an invariant mass in the range $100 < m_{\gamma\gamma} < 180$ GeV, for both data and simulated background events passing the preselection. The $\mathrm{BDT}_{\gamma\,\mathrm{ID}}$ score is also shown for electrons reconstructed as photons in $\mathrm{Z} \to \mathrm{e}^+\mathrm{e}^-$ events, in data and simulation. The systematic uncertainty on the photon identification output, represented by the hashed region in Fig. 4 (b), has been conservatively estimated as a shift of ± 0.03 of the score plus a linearly increasing term to cover any differences between data and simulation, in particular at low photon identification scores.

A very loose requirement is applied on the $\mathrm{BDT}_{\gamma\,\mathrm{ID}}$ score of both photons. The efficiency of the loose photon identification requirements and preselection is measured in data using a tag and probe technique [26]. The efficiency of the complete selection, excluding the electron veto requirement, is determined using $\mathrm{Z} \to \mathrm{e}^+\mathrm{e}^-$ events. Table 2 shows the results for data and simulation, and the ratio of efficiency in data to that in the simulation, $\epsilon_{data}/\epsilon_{sim}$.

The photon selection efficiency of the electron veto requirement is assessed using $\mathrm{Z} \to \mu^+\mu^-\gamma$ events, where the photon is produced by final-state radiation (FSR), which provides a $> 99\%$ pure source of prompt photons. The efficiency of the electron veto selection ranges from 96% to 100% and the ratio $\epsilon_{data}/\epsilon_{sim}$ is compatible to unity within the uncertainties in all categories. Statistical and systematic uncertainties for the measurements of efficiencies using data are propagated to the uncertainties on the ratios. The ratios are used as corrections to the signal efficiency in the simulation and the uncertainties on the ratios are taken as systematic uncertainties.

Using a tag-and-probe method on $Z \to e^+e^-$ events, we find the overall trigger efficiency of the diphoton system after preselection to be around 95%. In this measurement of the efficiency, the R_9 distribution was reweighed to match photons from $H \to \gamma\gamma$. The measured efficiencies have been used as a scale factor for the simulation and their uncertainties used as systematic uncertainties.

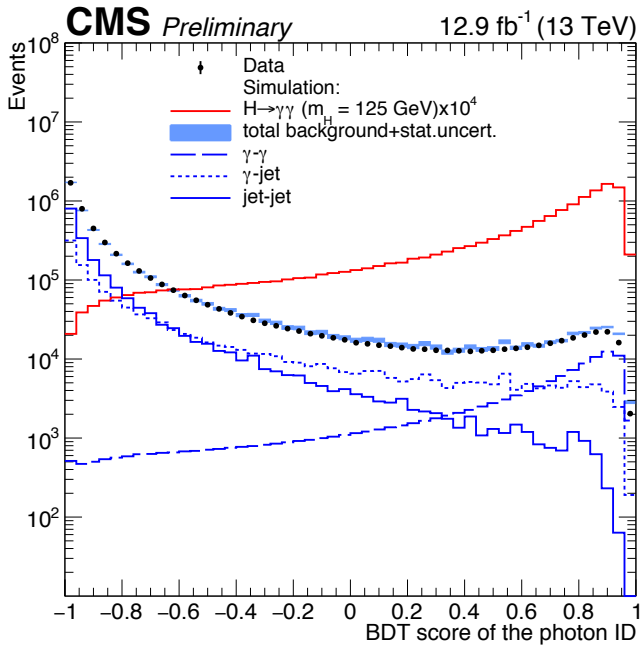

(a)

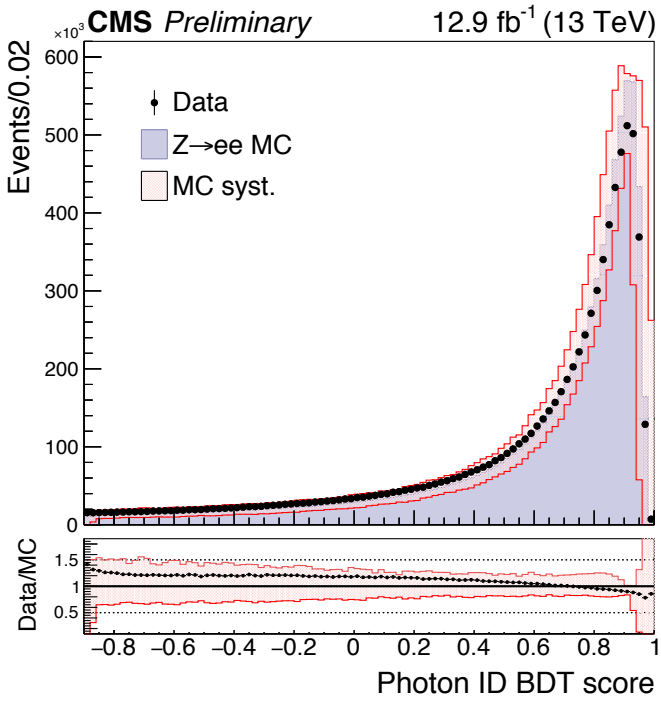

(b)

Figure 4: (a) $\mathrm{BDT}_{\gamma\,\mathrm{ID}}$ score of the lower-scoring photon of diphoton pairs with an invariant mass in the range $100 < m_{\gamma\gamma} < 180$ GeV, for events passing the preselection in the 13 TeV dataset (points), and for simulated background events (blue histogram). Histograms are also shown for different components of the simulated background, in which there are either two, one, or zero prompt candidate photons. The sum of all background distributions, generated at leading order, is scaled up to data. The red histogram corresponds to simulated Higgs boson signal events. (b) $\mathrm{BDT}_{\gamma\,\mathrm{ID}}$ score for $\mathrm{Z} \to \mathrm{e}^{+}\mathrm{e}^{-}$ events in data and simulation, where the electrons are reconstructed as photons. The systematic uncertainty applied to the shape from simulation (hashed region) is also shown.

	DATA			Simulation		Ratio	
	Eff.	Stat. Unc.	Syst. Unc.	Eff.	Stat. Unc.	Eff.	Unc.
ECAL Barrel; R_9 >0.85	0.9451	0.0006	0.0192	0.9374	0.0007	1.0080	0.0192
ECAL Barrel; R_9 <0.85	0.8255	0.0012	0.0119	0.8258	0.0009	0.9960	0.0120
ECAL Endcap; R_9 >0.90	0.9099	0.0008	0.0212	0.9127	0.0010	0.9969	0.0212
ECAL Endcap; R_9 <0.90	0.4993	0.0018	0.0249	0.5024	0.0016	0.9938	0.0250

Table 2: Photon preselection efficiencies measured in four photon categories, obtained with a tag and probe technique using $Z \to e^+e^-$ events after applying all requirements except the electron veto.

6 Diphoton selection

For events passing the selection, a multivariate classifier is trained to separate $H \to \gamma\gamma$ candidates from diphoton background. The event classifier, labelled as $BDT_{\gamma\gamma}$, gives a high score to events with signal-like kinematic characteristics, good diphoton mass resolution and photon-like values from $BDT_{\gamma\,ID}$. Setting requirements on the $BDT_{\gamma\gamma}$ output allows the definition of categories with different sensitivities. The categorisation scheme is described in detail in Section 7. The variable is designed to be mass independent. This is achieved by choosing a set of inputs of the BDT such that the mass of simulated signal samples used for training sample cannot be inferred.

The variables used as inputs to the $BDT_{\gamma\gamma}$ are:

- the relative transverse momenta of both photons, $p_T^{1(2)}/m_{\gamma\gamma}$;
- the pseudorapidities of both photons, $\eta^{1(2)}$;
- the cosine of the angle between the two photons in the transverse plane, $\cos(\phi_1 - \phi_2)$;
- the relative diphoton mass resolution, under the hypothesis that the mass has been reconstructed using the correct primary vertex, $\sigma_m^{right}/m_{\gamma\gamma}$;
- the relative diphoton mass resolution, under the hypothesis that the mass has been reconstructed using an incorrect primary vertex, $\sigma_m^{wrong}/m_{\gamma\gamma}$;
- the per-event probability estimate that the correct primary vertex has been used to reconstruct the mass, taken from $BDT_{VTX\,PROB}$;
- the $BDT_{\gamma\,ID}$ score for both photons.

The choice of inputs is justified by the fact that the diphoton mass resolution depends on the geometrical location of the associated energy deposits in the calorimeter; the kinematics of the diphoton system ; the quality of the individual photons (e.g. if they converted in from of the ECAL); and the probability that the correct primary vertex has been used to reconstruct the diphoton mass.

The $BDT_{\gamma\gamma}$ is trained with signal events weighted proportionally to the inverse of the right and wrong vertex resolutions. This way, events with a better mass resolution will tend to be assigned a higher $BDT_{\gamma\gamma}$ score. The training is performed using simulated samples for the three main background components (prompt-prompt, prompt-fake and fake-fake) and Higgs boson simulated signal events with $m_H = 125$ GeV. The samples are statistically independent from those used to build the signal model (Section 8).

The distributions of the $BDT_{\gamma\gamma}$ input variables and its output in simulation and data are compared using $Z \to e^+e^-$ events. Fig. 5 (left) shows the $BDT_{\gamma\gamma}$ output distribution for data and

simulated background events in the region $100 < m_{\gamma\gamma} < 180$ GeV. The output of the BDT has been transformed in order to have a flat distribution for the signal events. The vertical lines represent the boundaries of the categories used in the analysis and defined in Section 7. A factor of about 1.5, derived preserving the relative ratio of the single components, is applied to simulation. This normalization is not used anywhere else in the analysis. Fig. 5 (right) shows the agreement between data and simulation of the transformed $\mathrm{BDT}_{\gamma\gamma}$ score in $Z \to e^+e^-$ events where electrons are reconstructed as photons. The two main sources of systematic uncertainty on the diphoton discriminant arise from $\mathrm{BDT}_{\gamma\,\mathrm{ID}}$ score and from the per-photon energy resolution estimate from the energy regression (to which a 5% uncertainty is assigned in both barrel and endcaps). The impact of these two systematic uncertainties on the $\mathrm{BDT}_{\gamma\gamma}$ score is represented as the shaded band. Data and simulation agree within uncertainties in the whole range except in the low score region, whose events are removed from the analysis anyway. The unused region is indicated with grey shading. The discrepancy can be explained by residual background contamination and by differences in the photon identification discriminant between data and simulation for photons having low value of the $\mathrm{BDT}_{\gamma\,\mathrm{ID}}$.

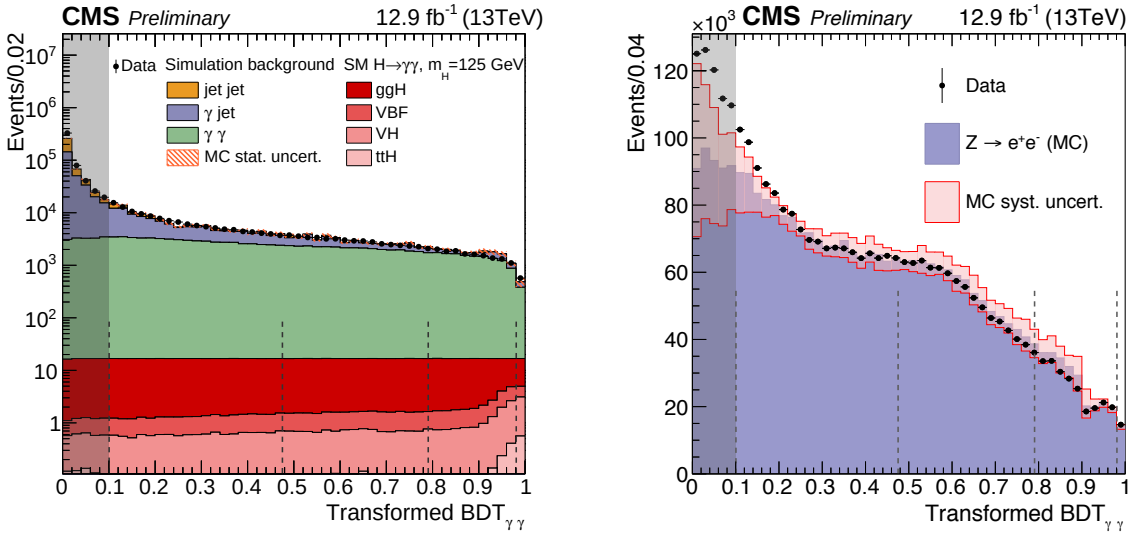

Figure 5: (Left) Transformed $\mathrm{BDT}_{\gamma\gamma}$ classifier score in data (black points) and simulation (stacked histograms) for events in the region $100 < m_{\gamma\gamma} < 180$ GeV. (Right) Transformed $\mathrm{BDT}_{\gamma\gamma}$ classifier score for $Z \to e^+e^-$ events, where electrons are reconstructed as photons, in data (black points) and simulation (filled histogram). The hashed region represents the systematic uncertainty resulting from the combination of the uncertainties on the $\mathrm{BDT}_{\gamma\,\mathrm{ID}}$ and the photon energy resolution. The gray bands represent events rejected in the analysis.

7 Event categorisation

To improve the sensitivity of the analysis, events are categorized according to their mass resolution and signal-to-background ratio (using the $\mathrm{BDT}_{\gamma\gamma}$ output score), and most probable production mechanism. In this analysis, specific event categories are defined targeting Higgs boson production mechanisms other than gluon fusion (ggH): Higgs bosons production by vector boson fusion (VBF) mechanism and in association with top quark ($t\bar{t}H$) pairs. Higgs bosons produced by VBF are accompanied by a pair of jets separated by a large rapidity gap. Those produced via $t\bar{t}H$ are accompanied by two b quarks and two W bosons, and may be accompanied by charged leptons (e, μ) or additional jets.

The tagging of dijet events, for VBF, significantly increases the overall sensitivity of the analysis and the precision on the measured signal strength. The tagging aimed at the associated $t\bar{t}H$ production increases the sensitivity of the analysis to the coupling of the Higgs boson to the top quark. The diphoton p_T spectrum, and consequently the leading photon p_T spectrum, are harder in the case of the VBF and $t\bar{t}H$ processes than in the cases of the ggH process and of the non-resonant diphoton production. Various event categories are defined and organised in hierarchy, such that events are assigned exclusively to one category. First, a category aiming at selecting events originating from leptonic or semi-leptonic top decays is defined with the following requirements:

- leading photon $p_T > m_{\gamma\gamma}/2$;
- sub-leading photon $p_T > m_{\gamma\gamma}/4$;
- at least one lepton with $p_T > 20$ GeV: electrons must be within the ECAL fiducial region and pass loose requirements on the same observables as described in [27]. In addition the electron should satisfy $|m(e,\gamma) - m_Z| > 10$ GeV, where m_Z refers to the Z boson mass. Muons are required to have $|\eta| < 2.4$ and to pass a tight selection based on the quality of the track, the number of hits in the tracker and muon system, and the longitudinal and transverse impact parameters of the track with respect to the muon vertex; additionally, it has to satisfy a requirement on the relative isolation with pileup correction, based on the transverse momentum of the charged hadrons, transverse energy of the neutral hadrons and photons in a cone of radius 0.4 around the muon;
- all selected leptons (ℓ) are required to have $\Delta R(\ell,\gamma) > 0.4$;
- at least two jets in the event with $p_T > 25$ GeV, $|\eta| < 2.4$, and $\Delta R(\text{jet},\gamma) > 0.4$ and $\Delta R(\text{jet},\ell) > 0.4$;
- at least one of the jets in the event has to be identified as b jet according to the CSV tagger medium requirement [28];
- the diphoton must pass a loose requirement on the value of the $\text{BDT}_{\gamma\gamma}$ output.

Then jets from hadronic top decays are selected to define the $t\bar{t}H$ hadronic category, requiring:

- leading photon $p_T > m_{\gamma\gamma}/2$;
- sub-leading photon $p_T > m_{\gamma\gamma}/4$;
- no leptons defined according to the leptonic tag;
- at least five jets in the event with $p_T > 25$ GeV and $|\eta| < 2.4$;
- at least one of the jets in the event has to be identified as a b-jet according to the CSV tagger medium requirement [28];
- a minimum value of $\text{BDT}_{\gamma\gamma}$ output. The value is a compromise between significance optimisation and the need of a minimum number of events to fit the background.

Events with two jets and not selected by the previous criteria are divided into categories to target the VBF process. The procedure to define these categories closely follows the one used in the Run 1 analysis [9]. In order to be tagged as VBF-like, the events are preselected according to the following requirements:

- two jets with $p_T^{j_1} > 30$ GeV and $p_T^{j_2} > 20$ GeV and $|\eta| < 4.7$;
- $m_{j_1 j_2} > 250$ GeV.

In addition, a selection on the width of the jet $< R^2 >$ is introduced. This is required to be less

than 0.03 as described in Section 3.

A tight and loose category are created using a BDT classifier, labelled as $\mathrm{BDT}_{jj\gamma\gamma}$. The $\mathrm{BDT}_{jj\gamma\gamma}$ is built using a kinematic dijet BDT (labelled as BDT_{jj}), the $\mathrm{BDT}_{\gamma\gamma}$, and $p_{\mathrm{T}}^{\gamma\gamma}/m_{\gamma\gamma}$ as inputs. The separation of the multivariate VBF analysis into two steps is crucial to correctly discriminating against both background and Higgs boson signal from other production modes. The BDT_{jj} is trained to identify likely VBF events using kinematic properties of the jets, and so considers gluon-gluon fusion Higgs boson events as background. However the $\mathrm{BDT}_{jj\gamma\gamma}$ also considers the diphoton quality, and it would not behave correctly if the gluon-gluon fusion Higgs boson events were treated as a background because it would not treat high-quality diphotons as signal-like. The two-BDT categorisation is able to take advantage of the VBF identification power of BDT_{jj} as well as the diphoton identification power of the $\mathrm{BDT}_{\gamma\gamma}$.

The BDT_{jj} is built using dijet and diphoton kinematic quantities: the transverse momenta of the leading and sub-leading photons divided by $m_{\gamma\gamma}$, the transverse momenta of the leading and sub-leading jets, the difference in pseudorapidity between the two jets $\Delta\eta_{j_1j_2}$, the dijet invariant mass $m_{\mathrm{j_1j_2}}$, the Zeppenfeld variable [29] and the difference in azimuthal angle between the dijet and the diphoton $\Delta\phi(\mathrm{j_1j_2}, \gamma\gamma)$. Because of the large theoretical uncertainty in the ggH + 2 jets cross section in the region very close to $\Delta\phi(\mathrm{j_1j_2}, \gamma\gamma) = \pi$, the maximum value of the variable is restricted to $\pi - 0.2$, and events with $\Delta\phi(\mathrm{j_1j_2}, \gamma\gamma) > \pi - 0.2$ are treated as if the value was $\pi - 0.2$. The ratio $p_{\mathrm{T}}^{\gamma\gamma}/m_{\gamma\gamma}$ is included as an input because of its significant correlation to both the BDT_{jj} and the $\mathrm{BDT}_{\gamma\gamma}$.

The tight and loose categories are defined as bins in $\mathrm{BDT}_{jj\gamma\gamma}$ output. The locations of the bin boundaries are optimised by first choosing the requirement that maximizes the signal significance in the tight bin, then repeating the procedure for the loose bin. The remaining inclusive events are split using the diphoton multivariate classifier, $\mathrm{BDT}_{\gamma\gamma}$, using information from the photon kinematics, the mass resolution, and the signal to background ratio. The position of the boundaries of the categories in the $\mathrm{BDT}_{\gamma\gamma}$ output spectrum is chosen to minimize the combination of the p-values extracted from a fit to an Asimov toy dataset [30] generated from the signal+background model. An optimal number of four categories is found, with boundaries defined as requirements on the $\mathrm{BDT}_{\gamma\gamma}$ output score, as seen in Fig. 5. Events with a $\mathrm{BDT}_{\gamma\gamma}$ score lower than the lowest threshold are discarded.

As a summary, events are sorted into eight categories (or "tags"), loosely corresponding to Higgs boson production modes and labelled as: TTH Leptonic Tag, TTH Hadronic Tag, VBF Tag 0, VBF Tag 1, Untagged 0, Untagged 1, Untagged 2 and Untagged 3. The "VBF" and "Untagged" categories are labelled from best resolution to worst.

8 Signal model

Interpreting the data recorded by CMS requires a description of the expected signal for a standard model Higgs boson which includes the overall number of events as a function of m_{H} and the shape of the distribution of $m_{\gamma\gamma}$ in each category. A parametrised model of the Higgs boson mass shape continuously varying between 120 and 130 GeV is obtained from simulation. This includes all the necessary tuning to the simulation as well as all the corrections for the relevant efficiencies measured in data. The chosen approach is to describe the signal model with an analytic function, whose parameters are determined by fitting the simulated events in each category and for each of the simulated Higgs boson mass points.

Since the distribution of $m_{\gamma\gamma}$ changes considerably depending on whether the vertex associated

with the candidate diphoton was correctly identified within 1 cm, distributions where the right vertex (RV) and wrong vertex (WV) were chosen are fit separately when constructing the signal model. For each process, category and RV/WV scenario, the $m_{\gamma\gamma}$ distributions are fitted using a sum of at most five Gaussian functions. The number of Gaussian functions is chosen as the minimum number required to give a reasonable fit.

The model is constructed by interpolating each parameter between individual mass points using a spline. Seven mass points are used for this purpose: m_H =120, 123, 124, 125, 126, 127, and 130 GeV. The analytic functions for each production mode are summed together, weighted by their relative cross sections, to obtain the final function in each category. Fig. 6 shows the signal model corresponding to $m_H = 125$ GeV for the best resolution category and also for all categories combined together. The efficiency $\times$ acceptance of the signal model as a function of m_{H} for all categories combined is shown in Fig. 7. The yellow band indicates the effect of the systematic uncertainties for: trigger; photon identification and selection; photon energy scale and tuning of the energy resolution in the simulation; vertex identification (see Section 10).

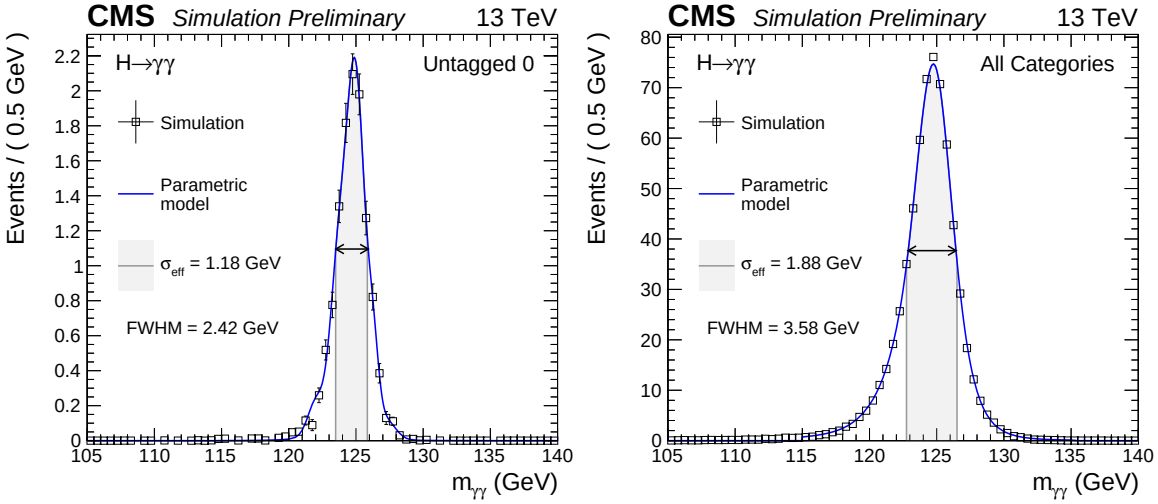

(a) (b)

Figure 6: Parametrized signal shape for the best resolution category (left) and for all categories combined together (right) for a simulated H $\rightarrow \gamma\gamma$ signal sample with $m_{\mathrm{H}} = 125$ GeV. The black points represent weighted simulation events and the blue lines are the corresponding models. Also shown are the σ_{eff} value (half the width of the narrowest interval containing 68.3% of the invariant mass distribution), FWHM and the corresponding interval.

9 Background model

The model used to describe the background is extracted from data with the discrete profiling method [31]. This technique was designed as a way to estimate the systematic uncertainty associated with choosing a particular analytic function to fit the background $m_{\gamma\gamma}$ distribution. The method treats the choice of the background function as a discrete parameter in the likelihood fit to the data. The resulting systematic uncertainty is then calculated in an analogous way to systematic uncertainties associated with other contributions.

A large set of candidate function families is considered, including exponentials, Bernstein polynomials, Laurent series and power law functions. An F-test is performed to determine the

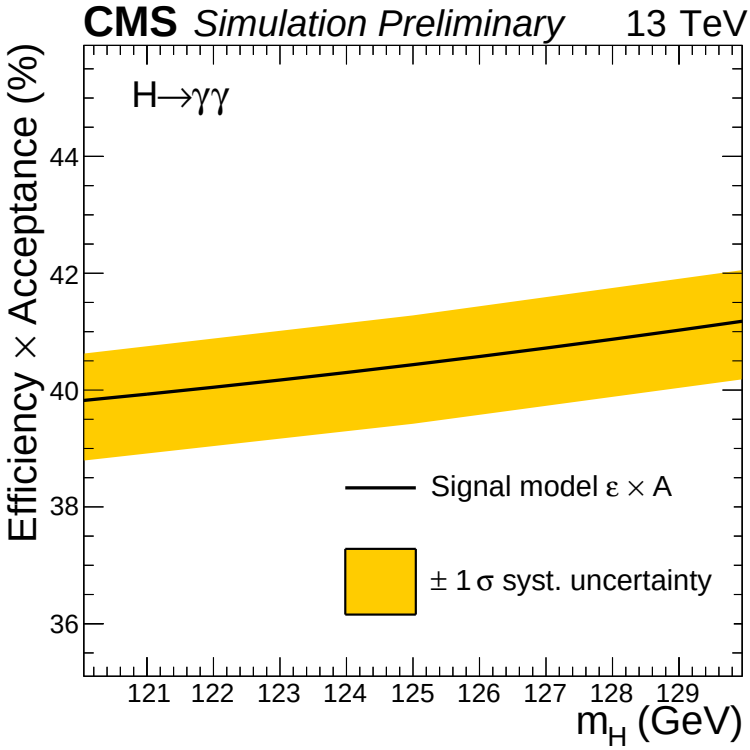

Figure 7: The efficiency $\times$ acceptance of the signal model as a function of m_{H} for all categories combined.

maximum order for each family function that can be used in the discrete profiling method. A goodness of fit test is applied to remove lower order functions which are not suitable to fit the data.

When fitting these functions to the background $m_{\gamma\gamma}$ distribution, the value of twice the negative logarithm of the likelihood (2NLL) is minimized. A penalty is added to 2NLL to take into account the number of floating parameters in each candidate function. When making a measurement of a given parameter of interest, the discrete profiling method determines the envelope of the lowest values of 2NLL profiled as a function of the parameter of interest.

10 Systematic uncertainties

The systematic uncertainties are treated differently depending on how they affect the $m_{\gamma\gamma}$ distribution. Uncertainties modifying the shape of the $m_{\gamma\gamma}$ distribution are built directly into the signal model as nuisance parameters. In cases where the shape of the $m_{\gamma\gamma}$ distribution is largely unaffected, the systematic variations are treated as log-normal uncertainties on the yield of a given category. For cases where the systematic has an effect on the input to one of the classification BDTs, the uncertainty takes the form of a variation on the category yield, representing category migration.

The systematic uncertainties considered in this analysis are the following:

- Theory systematic uncertainties:
  - *parton density functions (PDF) uncertainties*: This uncertainty is split into two types. Firstly, we consider the effect of the PDF uncertainty on the overall normalisation. Secondly, we consider the potential effect on the relative yield in each process and category. The overall normalisation uncertainties are computed from the PDF4LHC15 [32] combined PDF set, while the bin-to-bin shifts are calculated from [33] using the MC2hessian procedure [34]. The category migrations are found to be typically less than 2%, depending on the category.
  - α_s *uncertainty*: the uncertainty on the value of the strong force coupling constant α_s. Once again this is split between the overall effect on the normalisation and the category migration. The former is taken directly from [18] while the latter is evaluated following the same procedure as for the PDF uncertainty category migrations. The overall variation in the relative event yield due to the α_s uncertainty is at most 3.7%.
  - *Underlying event and parton shower uncertainty*, which is obtained using samples where the choice and tuning of the generator has been modified. This systematic uncertainty is treated as an event migration systematic as it will chiefly affect the jets in the analysis. The possibility that an event could move from one VBF Tag to another or from either VBF Tag to an inclusive category is assigned a systematic uncertainty of 7% and 9% respectively.
  - *QCD scale uncertainty*, related to varying the renormalization and factorization scales: the uncertainties are taken as variations on the QCD parameters μ_R and μ_F. The overall effect on the normalisation is taken from [18] and effect on the relative category yield is found to be about 5-10%.
  - *Uncertainty on the* $H\rightarrow\ \gamma\gamma$ *branching fraction*: is estimated to be about

2.08% [18].

- *Gluon fusion contamination in VBF and* $t\bar{t}H$ *tagged categories*: the theoretical predictions for gluon fusion are not reliable in a regime where the Higgs boson is produced in association to a large number of jets. The uncertainty on the yield of gluon fusion events in the VBF tagged classes has been estimated using the Stewart-Tackmann procedure following the recommendation of the LHC Higgs Cross Section Working Group [18]. The overall normalization has been found to vary by 39% while migrations between the two VBF categories are of about 10%. The systematic uncertainty on the gluon fusion contamination in the $t\bar{t}H$ tagged classes have been estimated taking into account several contributions:
  - uncertainty due to the limited size of the simulated sample: 10%.
  - uncertainty from the parton shower modelling. This uncertainty is estimated as the observed difference in the jet multiplicity between MADGRAPH5_aMC@NLO predictions and data in $t\bar{t}$ +jets events (which are dominated by gluon fusion production $gg \to t\bar{t}$), with fully leptonic $t\bar{t}$ decays. This uncertainty is about 45% in the bins with the largest discrepancy ($N_{\text{jets}} \geq 5$) [35].
  - uncertainty on the gluon splitting modelling. This is estimated by scaling the fraction of events from gluon fusion with real b-jets by the observed difference between data and simulation in the ratio $\sigma(t\bar{t}b\bar{b})/\sigma(t\bar{t}jj)$ at 13 TeV. This uncertainty implies a variation of about 18% in the yield of gluon fusion events.
- *Integrated luminosity* is estimated from data, and amounts to a 6.2% uncertainty on the signal yield.
- *Trigger efficiency*: the trigger efficiency is measured from $Z \to e^+e^-$ events using the tag-and-probe technique; the size of the effect on the event yields is of less than 0.1%.
- *Photon preselection*: the systematic uncertainty is taken as the uncertainty on the ratio between the efficiency measured in data and in simulation; it ranges from 0.1% to 2.3% according to the photon category and results in an event yield variation up to 4% depending on the event category.
- *Vertex finding efficiency*: the largest contribution to the uncertainty comes from the modelling of the underlying event, plus the uncertainty on the ratio of data and simulation obtained using $Z \to \mu^+\mu^-$ events. It is handled as an additional nuisance parameter built into the signal model which allows the fraction of events in the right vertex/wrong vertex scenario to change. The size of the uncertainty of the vertex selection efficiency is 1.5%.
- *Energy scale and resolution*: scale and resolutions are studied with electrons from $Z \to e^+e^-$ and then applied to photons. The main source of systematic uncertainty is the different interactions of electrons and photons with material upstream the ECAL. Uncertainties are assessed by changing the R_9 distribution, the regression training (using electrons instead of photons) and the electron selection used to derive the corrections. The uncertainty on the additional energy smearing is assigned propagating the uncertainties on the various $|\eta|$ and R_9 bins to the Higgs boson signal phase space. In both cases dedicated nuisance parameters are included as additional systematic terms in the signal model and amount to a 0.15% to 0.5% effect on the

photon energy depending on the photon category. The effect of the measurement of the signal strength is found to be of order 6%.

- *Non-uniformity of the light collection*: The uncertainty on the response of the ECAL crystals. The uncertainty has been slightly amplified with respect to Run 1 toaccount for the effect of larger transparency loss of the ECAL crystals. The size of the effect on the photon energy scale for 2016 data is estimated to be 0.07%.
- *Non-linearity*: The uncertainty associated with the non-linearity of the photon energy between MC simulation and data. This effect is estimated using Z boson decays to electron-positron pairs. The effect is found to be 0.1% on the photon energy in all categories, except Untagged 0 in which is is 0.2%
- *Geant4*: A further small uncertainty is added to account for imperfect electromagnetic shower simulation in GEANT 4 [20]. A simulation made with an improved shower description, changes the energy scale for both electrons and photons. Although mostly consistent with zero, the variation is interpreted as a limitation on our knowledge of the correct simulation of the showers, leading to a further uncertainty of 0.05% on the photon energy.
- *Modeling of the material budget*: The uncertainty on material budget between the interaction point and the vertex, which affects the behaviour of electrons and photons showers, is estimated with special simulation samples where the material budget is uniformly varied by ± 5 %. The effect on the energy scale is at most 0.17%.
- *Shower Shape Corrections*: The uncertainty deriving from the imperfect shower shape modelling in simulation. It is estimated using simulated $H \to \gamma\gamma$ and $Z \to e^+e^-$ samples with and without shower shape corrections. The effect on the photon energy scale is found to be at most 0.064%.
- *$BDT_{\gamma\, ID}$ score*: in order to cover the observed discrepancies between data and simulation, the uncertainty on the signal yields in the different categories of the analysis is estimated conservatively by propagating the uncertainty described in Section 5.
- *Per-photon energy resolution estimate*: this uncertainty is parametrised conservatively as a rescaling of the resolution estimate by $\pm 5\%$ about its nominal value, in order to cover all data/simulation differences in the distribution of the estimator output. More details can be found in the discussion on the energy regression BDT listed in Section 3.
- *Jet energy scale and smearing corrections*: this uncertainty is implemented as migration within VBF categories, within $t\bar{t}H$ categories and from tagged to untagged categories. Jet energy scale corrections account for a 4-15% migration within VBF categories and 4-15% from VBF to untagged categories. Migration due to energy scale in $t\bar{t}H$ categories is about 5%. The jet energy resolution has a smaller impact on the event migration, which is of less than 2% for all migrations.
- *b-tagging efficiency*: this uncertainty is evaluated by varying the ratio between the measured b-tagging efficiency in data and simulation within their uncertainty [28]. The resulting uncertainty on the signal yield is about 2% in the lepton-tagged category and 5% in the hadronic-tagged category.
- *Lepton identification*: for both electrons and muons, the uncertainty is computed by varying the ratio of the efficiency measured in data and simulation by its uncertainty. The resulting differences in the selection efficiency for the $t\bar{t}H$ category tagged by leptons, is less than 1%.

Event Categories	SM 125GeV Higgs boson expected signal								Bkg
	Total	ggh	vbf	wh	zh	tth	σ_{eff}	σ_{HM}	(GeV^{-1})
Untagged Tag 0	11.92	79.10 %	7.60 %	7.11 %	3.59 %	2.60 %	1.18	1.03	4.98
Untagged Tag 1	128.78	85.98 %	7.38 %	3.70 %	2.12 %	0.82 %	1.35	1.20	199.14
Untagged Tag 2	220.12	91.11 %	5.01 %	2.18 %	1.23 %	0.47 %	1.70	1.47	670.44
Untagged Tag 3	258.50	92.35 %	4.23 %	1.89 %	1.06 %	0.47 %	2.44	2.17	1861.23
VBF Tag 0	9.35	29.47 %	69.97 %	0.29 %	0.07 %	0.20 %	1.60	1.33	3.09
VBF Tag 1	15.55	44.91 %	53.50 %	0.86 %	0.38 %	0.35 %	1.71	1.40	22.22
TTH Hadronic Tag	2.42	16.78 %	1.28 %	2.52 %	2.39 %	77.02 %	1.39	1.21	1.12
TTH Leptonic Tag	1.12	1.09 %	0.08 %	2.43 %	1.06 %	95.34 %	1.61	1.35	0.42
Total	647.77	87.93 %	7.29 %	2.40 %	1.35 %	1.03 %	1.88	1.52	2762.65

Table 3: The expected number of signal events per category and the percentage breakdown per production mode in that category. The σ_{eff}, computed as the smallest interval containing 68.3% of the invariant mass distribution, and σ_{HM}, computed as the width of the distribution at half of its highest point divided by 2.35 are also shown as an estimate of the $m_{\gamma\gamma}$ resolution in that category. The expected number of background events per GeV around 125 GeV is also listed.

11 Results of the inclusive analysis

The data and the signal plus background model fit for each category used in this analysis are shown in Figs. 8, 9 and 10. The 1 standard deviation (green) and 2 standard deviation (yellow) uncertainty bands shown for the background component of the fit include the uncertainty in the fitted parameters.

Table 3 shows the expected number of signal events for each category. The total number is broken down by percentage contribution of each production mode to any particular event category. The σ_{eff} and σ_{HM} are also listed. The latter represents the width of the distribution at half of its highest point, divided by 2.35. The table also reports the expected number of background events per GeV in the corresponding σ_{eff} window around 125 GeV, which is taken from the best-fit candidate background parametrization.

The expected significance, the p-value, and the expected uncertainties on the measurement of signal strength ($\mu = \sigma_{obs}/\sigma_{SM}$, where σ_{obs} and σ_{SM} represent the observed and theoretical SM Higgs boson cross sections) for the observation of a standard model Higgs boson are obtained by generating an Asimov dataset [30] from the best-fit background model and injecting a signal of strength $\mu = 1$ at $m_H = 125$ GeV. The expected significance obtained after fitting using this procedure is show in Fig. 11, and the observed significance is also shown. The local expected significance for the observation of a standard model Higgs boson at $m_{\mathrm{H}} = 125.09$ GeV, i.e. the m_H resulting from CMS and ATLAS combination of measurements performed during Run 1, is 6.2 σ, where σ represents one standard deviation. The observed significance at $m_{\mathrm{H}} = 125.09$ GeV is 5.6 σ, and the maximum significance of 6.1 σ is observed at $m_{\mathrm{H}} = 126.0$ GeV.

A likelihood scan of the signal strength is performed, profiling all other nuisances. The results can be found in Fig. 12. In this scan, the mass of the Higgs boson mass was profiled in the same way as other nuisances in the fit. The best-fit signal strength measured for all categories combined using this method is $\widehat{\mu} = 0.95 \pm 0.20 = 0.95 \pm 0.17$ (stat.) $^{+0.10}_{-0.07}$ (syst.) $^{+0.08}_{-0.05}$ (theo.). If the Higgs boson mass is fixed to the Run 1 best-fit value $m_H = 125.09$ GeV, then the resulting signal strength is measured to be $0.91 \pm 0.20 = 0.91 \pm 0.17$ (stat.) $^{+0.09}_{-0.07}$ (syst.) $^{+0.08}_{-0.05}$ (theo.). Fig. 13 shows the signal strength separately for each of the categories used in the analysis. Fig. 14 shows the signal strength split by process. Since this analysis does not have any categories which specifically target the VH production mode, we set $\mu_{\mathrm{VH}} = 1$.

We define two signal-strength modifiers $\mu_{ggH,t\bar{t}H}$ and $\mu_{VBF,VH}$ as scale factors for the fermion

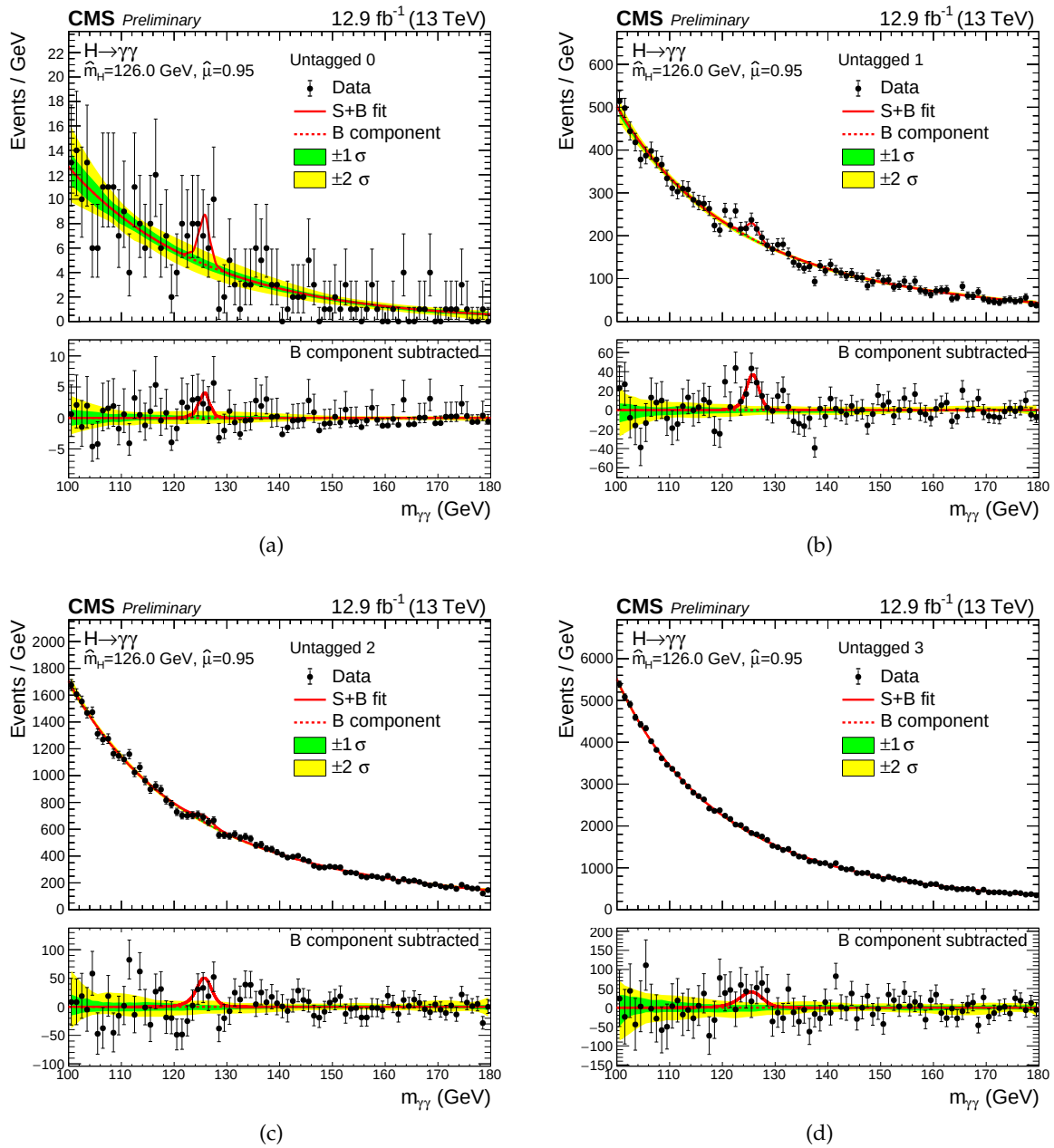

Figure 8: Data points (black) and signal plus background model fits in the four untagged categories are shown. The 1 standard deviation (green) and 2 standard deviation bands (yellow) include the uncertainties of the fit. The bottom plot shows the residuals after background subtraction.

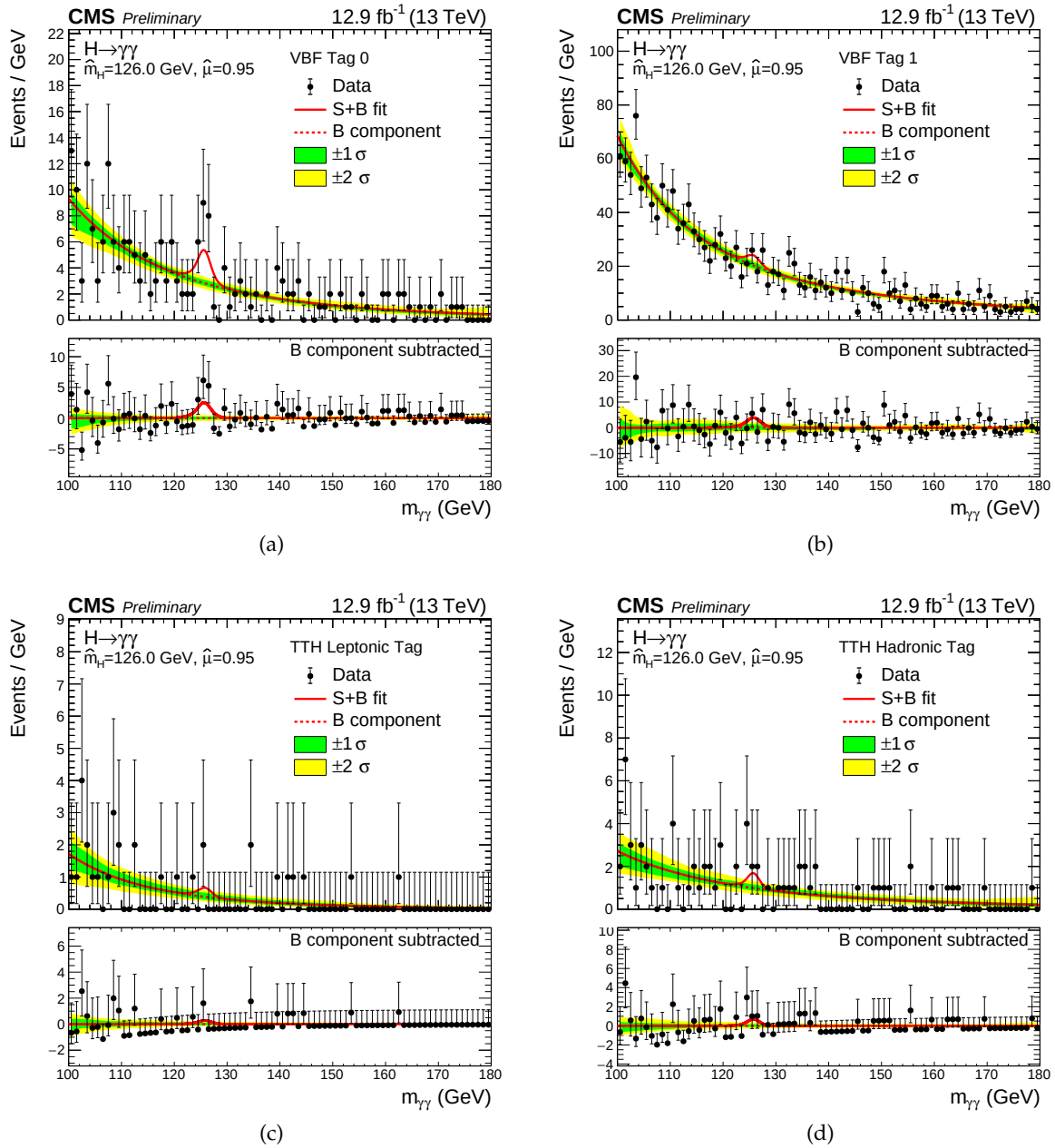

Figure 9: Data points (black) and signal plus background model fits in VBF and $t\bar{t}H$ categories are shown. The 1 standard deviation (green) and 2 standard deviation bands (yellow) include the uncertainties of the fit. The bottom plot shows the residuals after background subtraction.

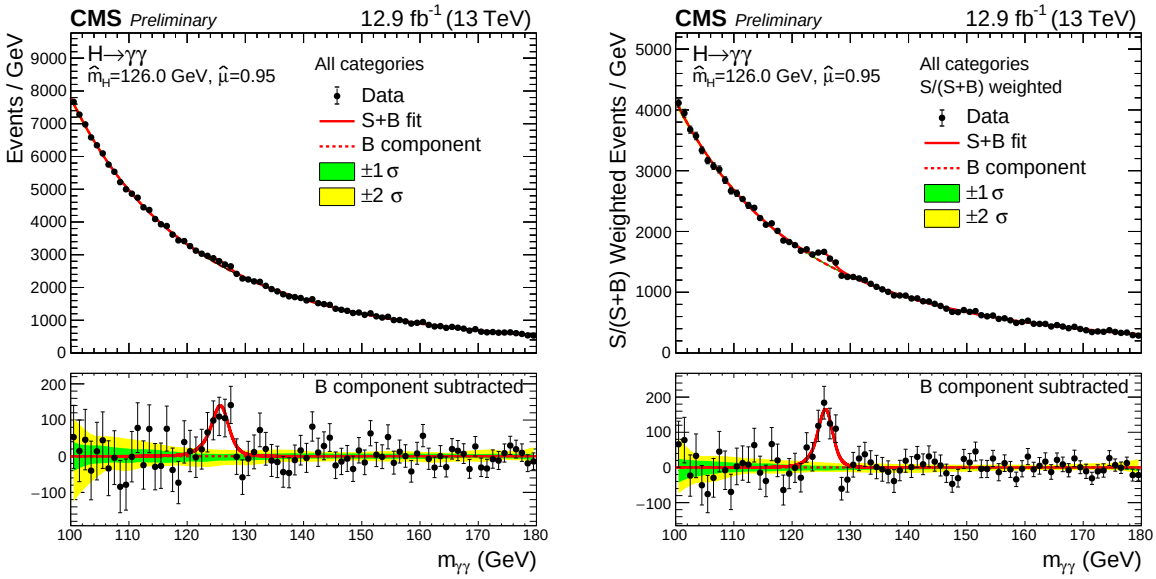

(a) (b)

Figure 10: Data points (black) and signal plus background model fits for all categories summed (left) and where the categories are summed weighted by their sensitivity (right). The 1 standard deviation (green) and 2 standard deviation bands (yellow) include the uncertainties of the fit. The bottom plot shows the residuals after background subtraction.

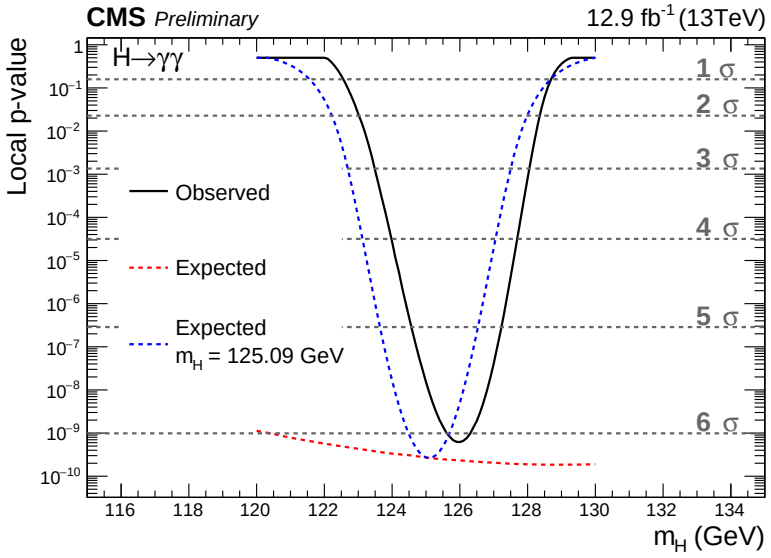

Figure 11: The observed p-value (black) is compared to the SM expectation across the fit range 120-130 GeV, where the SM Higgs boson is assumed to have a mass $m_H = 125.09$ GeV (blue). The red line shows the maximum significance for each mass hypothesis in the range 120 GeV $< m_H <$ 130 GeV.

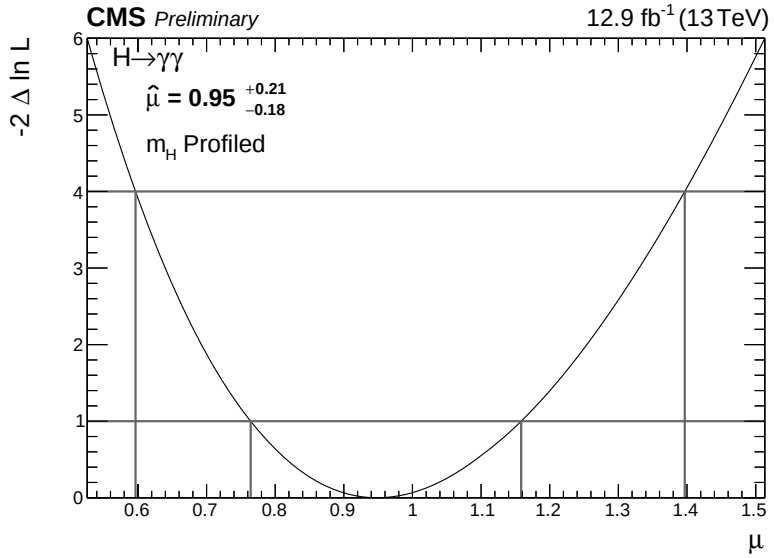

Figure 12: The likelihood scan for the signal strength where the value of the standard model Higgs boson mass is profiled in the fit.

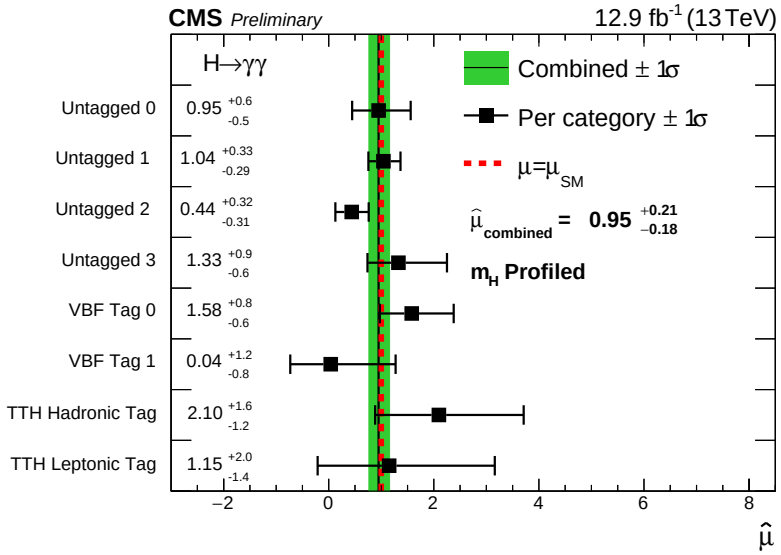

Figure 13: Signal strength modifiers measured in each category (black points) for profiled m_H, compared to the overall signal strength (green band) and to the SM expectation (dashed red line).

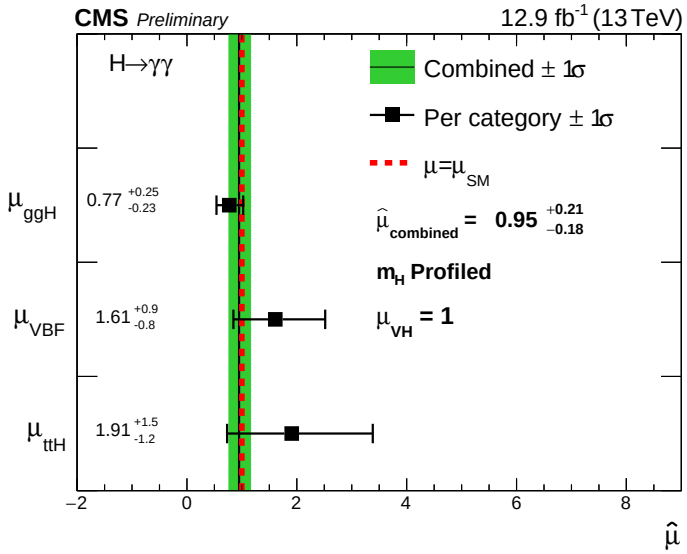

Figure 14: Signal strength modifiers measured for each process (black points) for profiled m_H, compared to the overall signal strength (green band) and to the SM expectation (dashed red line). Since this analysis does include any categories targeting the VH process, we impose $\mu_{\mathrm{VH}} = 1$.

(ggH $t\bar{t}H$ production modes) and vector-boson ((VBF, ZH, WH) production modes) induced contributions to the expected SM cross section. A two-dimensional likelihood scan of the signal strength $\mu_{ggH,t\bar{t}H}$ and $\mu_{VBF,VH}$ with the value of the parameter m_{H} profiled in the fit, is performed. Fig. 25 shows the 68% and 95% confidence level contours, the best-fit values are $\mu_{ggH,t\bar{t}H} = 0.80^{+0.14}_{-0.18}$ and $\mu_{VBF,VH} = 1.59^{+0.73}_{-0.45}$.

A scan of the Higgs boson mass, where the signal strength is profiled separately in its bosonic and fermionic components, is performed. The best fit mass is found at $m_H = 126.0$ GeV with statistical uncertainties of approximately 0.3 GeV. The systematic uncertainties are preliminarily estimated to be between 0.2 GeV and 0.4 GeV, and are still under study.

12 Fiducial cross section measurement

The fiducial cross section measurement follows the strategy defined in [9]. Relative to Section 7, the photon selection and event classification are modified to reduce their dependence on photon p_T and η, providing thereby a less model-dependent measurement. Furthermore, the absence of event categories targeting particular events tags, as VBF and $t\bar{t}H$ categories, further reduces the model-dependence of the categorisation. The selected events are categorized using an estimator of the mass resolution that is not correlated with $m_{\gamma\gamma}$. This simplifies the interpretation and the unfolding of the measurement, although it has a worse performance compared to the full event categorisation described in the previous sections, with a 30% worsening in the uncertainty on the expected signal strength. The $\mathrm{BDT}_{\gamma\gamma}$-based categorisation indeed combines information from a significantly higher number of variables in addition to mass resolution estimators.

The selection of events follows the description of Sections 3-5. Photons are required have a minimum $\mathrm{BDT}_{\gamma\,\mathrm{ID}}$ score tighter than the preselection requirement. The events are then categorised using a mass resolution estimator. The mass resolution estimator is obtained from a transfor-

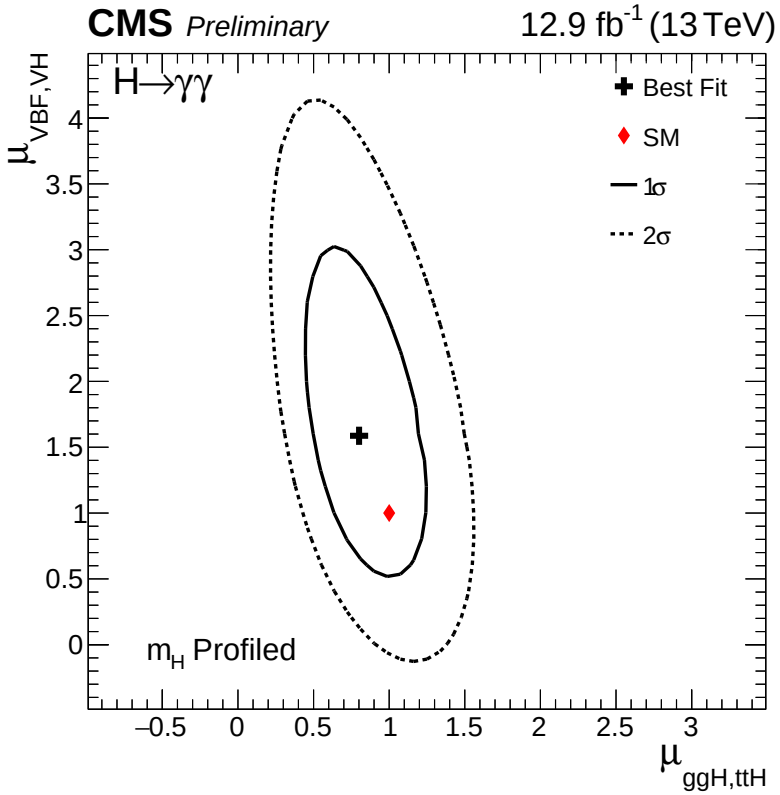

Figure 15: The two-dimensional best-fit (black cross) of the signal strengths for fermionic (ggH, $t\bar{t}H$) and bosonic (VBF, ZH, WH) production modes compared to the SM expectations (red diamond). The Higgs boson mass is profiled in the fit. The solid (dashed) line represents the 1 standard deviation (2 standard deviation) confidence region.

mation of the relative mass resolution σ_M/M, calculated under the assumption that the correct vertex was chosen, where σ_M represents the mass resolution. The transformation removes any correlation between the mass resolution and the mass itself, caused by the dependence of the energy resolution on the energy. The transformation is built using the cumulative distribution functions (CDFs) of the σ_M/M estimator in bins of the diphoton mass $m_{\gamma\gamma}$, using events from a $\gamma\gamma$ simulated sample. The transformation is derived separately for events where both photons are reconstructed in ECAL barrel region and for the remaining events. The transformed mass resolution estimator is then reinterpreted as a physical mass resolution by applying another transformation, using the inverse cumulative distribution function CDF(σ_M/M) calculated at $m_{\gamma\gamma} = 125$ GeV. The correlation of the mass resolution estimator with the pseudo-rapidities of the two photons is not removed by the transformation, allowing the use of the transformed variable to categorise events according to the typical mass resolution in a given region of the detector. The final decorrelated mass resolution estimator is referred to as $\sigma_M/M|_{\text{decorr}}$.

The definition of the event categories is achieved analogously to the "Untagged" categories described in Section 7. The optimal number of categories is found to be 3, whose boundaries correspond to values of $\sigma_M/M|_{\text{decorr}}$of 0, 0.0076, 0.0109,0.0288. Events with $\sigma_M/M|_{\text{decorr}}$exceeding the last boundary of the categorisation are discarded. Simultaneously to the category definition, the requirement on the minimum $\text{BDT}_{\gamma\,\text{ID}}$ score of both photons is optimised and set to 0.32.

Fig. 16 shows the $\sigma_M/M|_{\text{decorr}}$for electrons reconstructed as photons in $\text{Z} \to \text{e}^+\text{e}^-$ events, in data and simulation. The hashed region in Fig. 16, corresponds to the propagation of the systematic uncertainty on the per-photon energy resolution estimate (to which a 5% uncertainty is assigned in both barrel and endcaps) directly on the diphoton mass. The distributions are shown separately for events where both electrons are reconstructed in the ECAL barrel region (left) and for all remaining events (right). A discrepancy in the latter category between data and simulation is observed. The impact of this discrepancy on the cross section measurement, through migrations of signal events across categories, is found to produce a bias on the measurement of 2%, which is negligible compared to the statistical uncertainties.

The signal model is built using the same techniques employed in the main analysis, as described in Section 8. However, for the fiducial measurement, the signal model is built in each category inclusively for all production mechanisms, rather than for each process separately. The fiducial region is defined at generator-level with the following requirements:

- $\frac{p_{T,gen}^{\gamma_{1,(2)}}}{m_{\gamma\gamma}} > \frac{1}{3}(\frac{1}{4})$ for the generator-level transverse momentum of the leading (subleading) photon,
- $|\eta_{gen}^{\gamma}| < 2.5$ for the generator-level pseudorapidities of both photon
- the generator-level isolation of the photons, calculated as the sum of the transverse momenta of all stable particles inside a cone of aperture $R = 0.3$ around the photon, is required to be smaller than 10 GeV.

The signal model is constructed separately for events falling inside the fiducial volume, both at generator-level and reconstruction-level (inside-of-acceptance component, IA) and for events falling outside of the generator-level acceptance, but inside the reconstruction-level acceptance (outside-of-acceptance component, OA). The ratio between the fractions of reconstructed signal events falling outside-of-acceptance and inside-of-acceptance is 0.8%. The largest migration across the acceptance boundary occurs in the worst resolution category, where the ratio between outside- and inside-of-acceptance signal components amounts to 1.32%. Fig. 17 shows the parametrised signal shape for the best resolution category (left) and all categories combined

(right) for a simulated $H \to \gamma\gamma$ signal for $m_{\gamma\gamma} = 125$ GeV.

The background model is extracted in each mass resolution category with the data-driven technique described in Section 8. The signal plus background fits to the data are shown in Figs. 18 and 19. The 1 standard deviation (green) and 2 standard deviation (yellow) uncertainty bands shown for the background component of the fit include the uncertainty in the fitted parameters.

The fiducial cross section measurement is extracted through a simultaneous fit in the three categories in the acceptance region, performed while keeping the out-of-acceptance contamination fixed to the standard model prediction, thus unfolding the measurement to the generator-level acceptance through the subtraction of the outside-of-acceptance yield from the measured yield.

The measurement is compared to the standard model prediction, calculated as 1, where $\sigma_H^{th.}$ is the inclusive production cross section for a Higgs boson of 125.09 GeV and $BR(H_{\gamma\gamma})$ is its branching ratio in the $\gamma - \gamma$ channel, whose values are taken from [18]. The correct normalisation is restored by measuring the acceptance f_{acc}, defined as the ratio between the cross section relative to the generator fiducial volume and the total cross section, computed using MADGRAPH5_aMC@NLO and found to be 0.59. In summary, the fiducial cross section is obtained from the relation:

$$\sigma_{fid} = \sigma_H^{th.} \times BR_{\gamma\gamma} \times f_{acc} \tag{1}$$

The theoretical prediction based on the values in [18] and folding in the acceptance factor yields a value of 73.8 ± 3.8 fb for $m_H = 125.09$ GeV, being thus the expected fiducial cross section. The best fit fiducial cross section measured profiling the mass in the likelihood scan is found to be $\hat{\sigma}_{fid} = 69^{+18}_{-22}\text{fb} = 69^{+16}_{-22}(\text{stat.})^{+8}_{-6}(\text{syst.})\text{fb}$, as can be seen in Fig. 20.

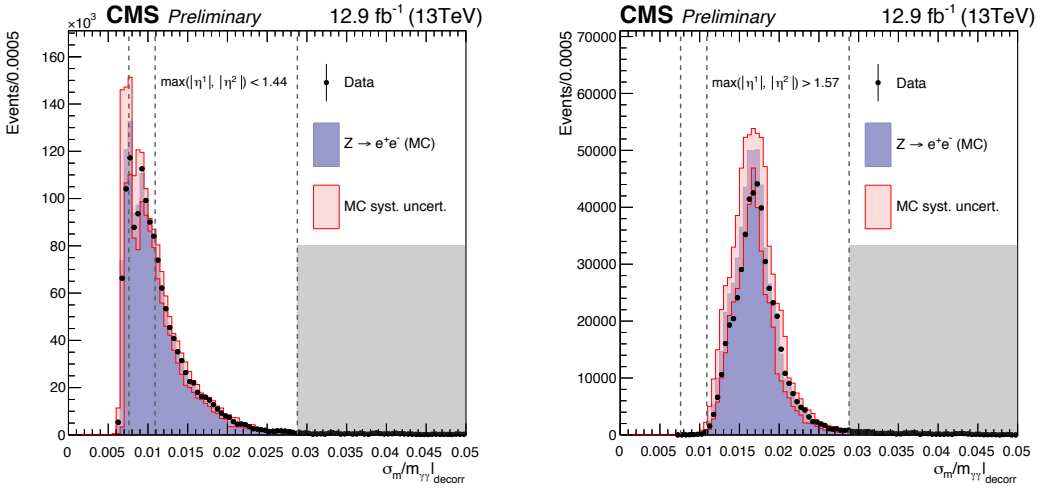

Figure 16: The distribution of the $\sigma_M/M|_{\text{decorr}}$ for $Z \to e^+e^-$ events, where electrons are reconstructed as photons, for events where both electrons are reconstructed in the ECAL barrel region (left) and for all remaining events (right). The red hashed region represents the systematic uncertainty resulting from the impact on the mass of the systematic uncertainty assigned to the per-photon energy resolution. Events in the gray region are discarded.

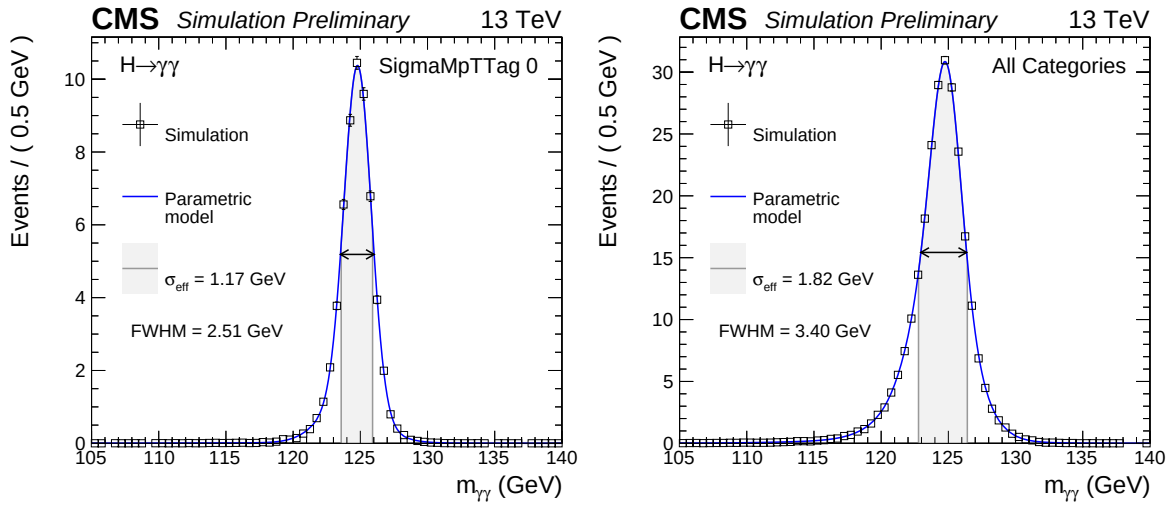

Figure 17: Fits of the distributions of the diphoton invariant mass for a simulated sample of Higgs bosons at $m_H = 125$ GeV for the category with the best resolution (left) and for all categories combined.

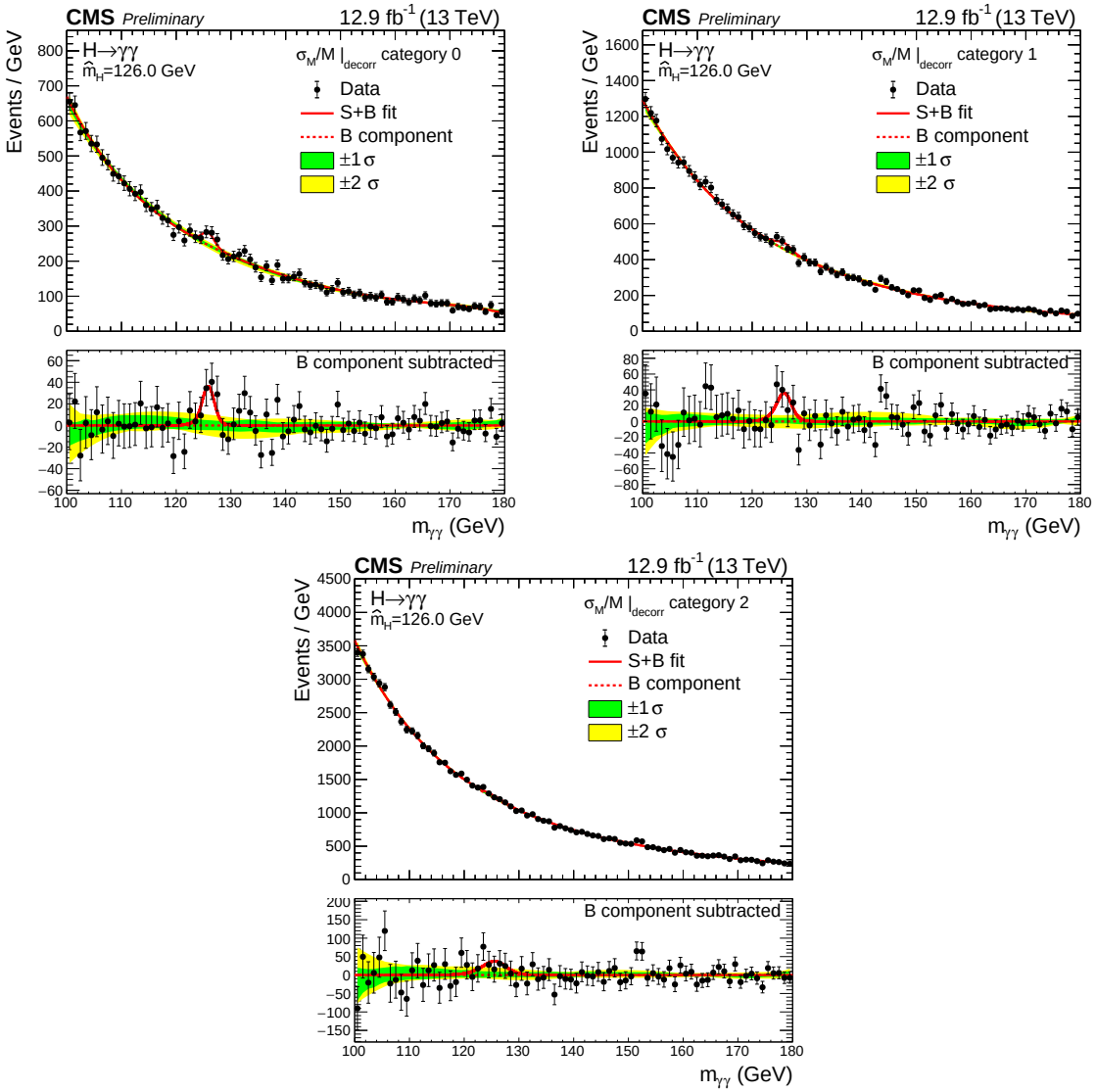

Figure 18: Data points (black) and signal plus background model fits in each of the categories used for the fiducial analysis are shown. The 1 standard deviation (green) and 2 standard deviation bands (yellow) include the uncertainties of the fit. The bottom plot shows the residuals after background subtraction.

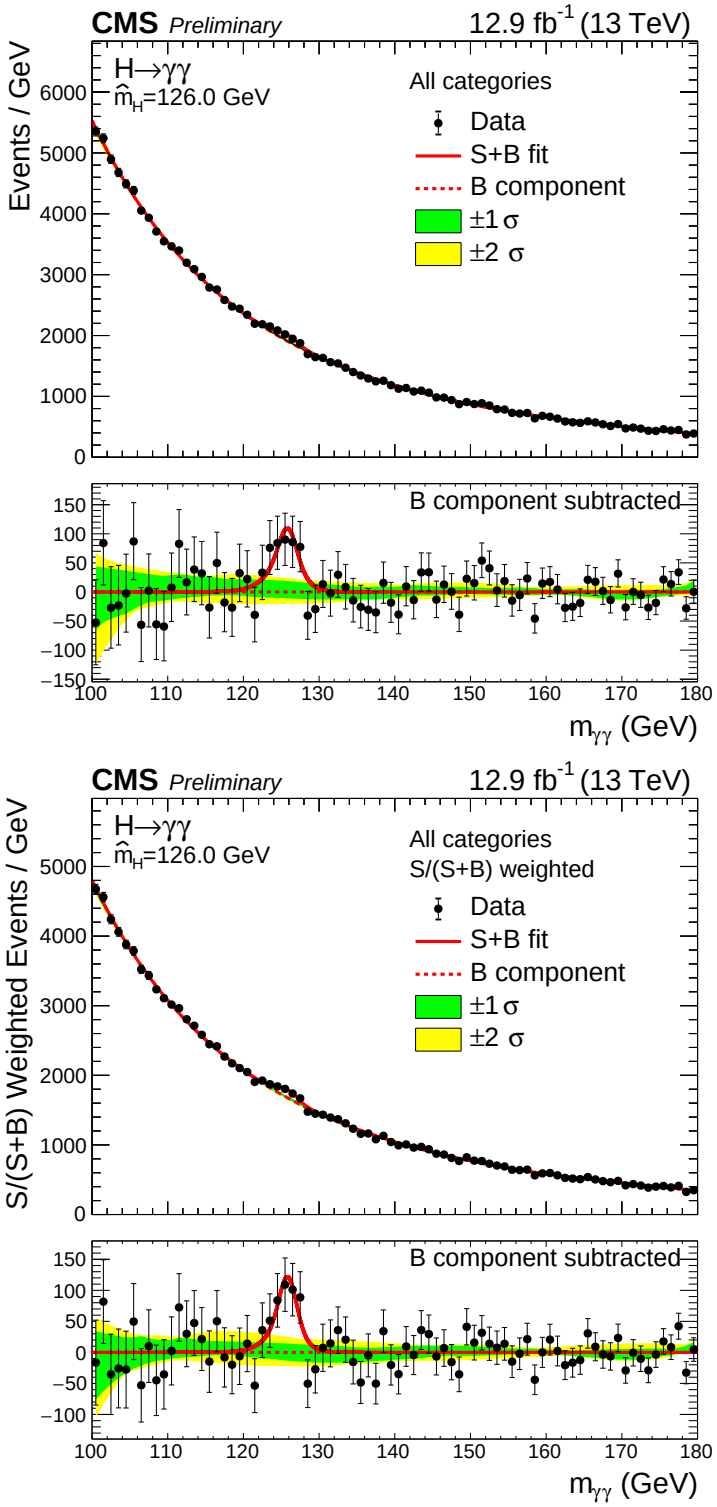

Figure 19: Data points (black) and signal plus background model fits for all the fiducial analysis categories summed (left) and where the categories are summed weighted by their sensitivity (right). The 1 standard deviation (green) and 2 standard deviation bands (yellow) include the uncertainties of the fit. The bottom plot shows the residuals after background subtraction.

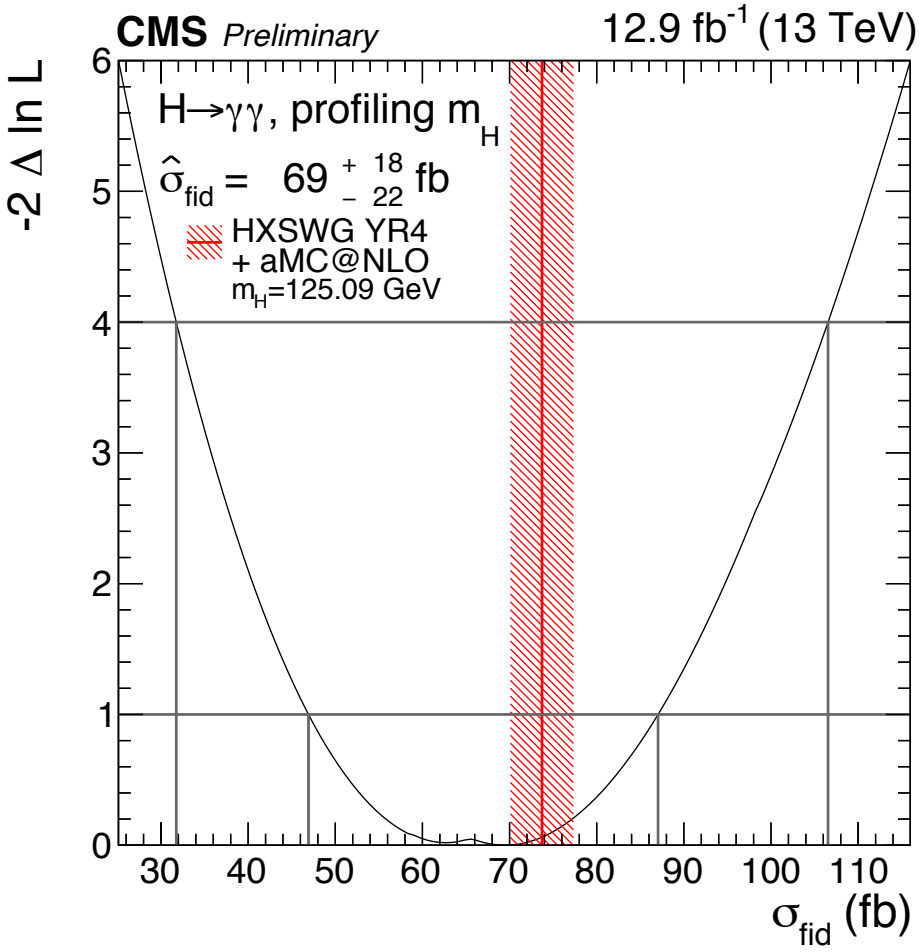

Figure 20: A likelihood scan for the fiducial cross section where the value of the standard model Higgs boson mass is profiled in the fit. The red line and hashed area represent the SM expected fiducial cross section and uncertainty for a Higgs boson of mass $m_H = 125.09$ GeV. The normalisation has been set using the latest values from [18] and the acceptance is defined using the aMC@NLO generator-level quantities.

13 Summary

We report the observation of the Higgs boson decaying in the diphoton channel and the measurement of some of its properties. The analysis uses the 2016 dataset so far collected by the CMS experiment in proton-proton collisions at $\sqrt{s} = 13$ TeV. The analysis follows closely the strategy adopted for the Run 1 result [9]. The selected events are divided into classes loosely targeting the different Higgs production processes, in order to increase the overall sensitivity of the analysis. A separate analysis making a measurement of the fiducial cross-section of the Higgs boson is also reported.

A clear signal is observed in the diphoton channel. The significance of the observation at the Run 1 best fit mass of $m_H = 125.09$ GeV is 5.6 σ where 6.2 σ was expected for the SM Higgs boson, and the best-fit signal strength fixing $m_H = 125.09$ GeV is reported to be $0.91 \pm 0.20 = 0.91 \pm 0.17$ (stat.) $^{+0.09}_{-0.07}$ (syst.) $^{+0.08}_{-0.05}$ (theo.). The best-fit values for the signal strength modifiers associated with the ggH and ttH production mechanisms, and with the VBF and VH mechanisms are found to be $\mu_{ggH,t\bar{t}H} = 0.80^{+0.14}_{-0.18}$ and $\mu_{VBF,VH} = 1.59^{+0.73}_{-0.45}$ respectively when m_H is profiled in the fit.

The highest significance of 6.1 σ was observed at $m_H = 126.0$ GeV, where 6.2 σ was expected.

The best-fit value of the fiducial cross section of the Higgs boson is found to be $\hat{\sigma}_{fid} = 69^{+18}_{-22}$fb $= 69^{+16}_{-22}$(stat.)$^{+8}_{-6}$(syst.)fb, where the standard model theoretical prediction is 73.8 ± 3.8 fb.

All the results are compatible with the expectations from a standard model Higgs boson.

References

[1] S. L. Glashow, "Partial-symmetries of weak interactions", *Nucl. Phys.* **22** (1961) 579, doi:10.1016/0029-5582(61)90469-2.

[2] S. Weinberg, "A model of leptons", *Phys. Rev. Lett.* **19** (1967) 1264, doi:10.1103/PhysRevLett.19.1264.

[3] A. Salam, "Weak and electromagnetic interactions", in *Elementary particle physics: relativistic groups and analyticity*, N. Svartholm, ed., p. 367. Almquvist & Wiskell, 1968. Proceedings of the eighth Nobel symposium.

[4] ATLAS Collaboration, "Observation of a new particle in the search for the Standard Model Higgs boson with the ATLAS detector at the LHC", *Phys. Lett.* **B716** (2012) 1–29, doi:10.1016/j.physletb.2012.08.020, arXiv:1207.7214.

[5] CMS Collaboration, "Observation of a new boson at a mass of 125 GeV with the CMS experiment at the LHC", *Phys. Lett.* **B716** (2012) 30–61, doi:10.1016/j.physletb.2012.08.021, arXiv:1207.7235.

[6] F. Englert and R. Brout, "Broken symmetries and the masses of gauge bosons", *Phys. Rev. Lett.* **13** (1964) 321, doi:10.1103/PhysRevLett.13.321.

[7] P. W. Higgs, "Broken symmetry and the mass of gauge vector mesons", *Phys. Rev. Lett.* **13** (1964) 508, doi:10.1103/PhysRevLett.13.508.

[8] G. Guralnik, C. Hagen, and T. Kibble, "Global Conservation Laws and Massless Particles", *Phys.Rev.Lett.* **13** (1964) 585, doi:10.1103/PhysRevLett.13.585.

[9] CMS Collaboration, "Observation of the diphoton decay of the Higgs boson and measurement of its properties", *Eur. Phys. J.* **C74** (2014), no. 10, 3076, doi:10.1140/epjc/s10052-014-3076-z, arXiv:1407.0558.

[10] ATLAS, CMS Collaboration, "Combined Measurement of the Higgs Boson Mass in pp Collisions at $\sqrt{s} = 7$ and 8 TeV with the ATLAS and CMS Experiments", *Phys. Rev. Lett.* **114** (2015) 191803, doi:10.1103/PhysRevLett.114.191803, arXiv:1503.07589.

[11] CMS Collaboration, "First results on Higgs to gammagamma at 13 TeV", Technical Report CMS-PAS-HIG-15-005, CERN, Geneva, 2016.

[12] CMS Collaboration, "The CMS experiment at the CERN LHC", *JINST* **3** (2008) S08004, doi:10.1088/1748-0221/3/08/S08004.

[13] CMS Collaboration, "Performance of Photon Reconstruction and Identification with the CMS Detector in Proton-Proton Collisions at sqrt(s) = 8 TeV", *JINST* **10** (2015), no. 08, P08010, doi:10.1088/1748-0221/10/08/P08010, arXiv:1502.02702.

[14] J. Alwall et al., "The automated computation of tree-level and next-to-leading order differential cross sections, and their matching to parton shower simulations", *JHEP* **07** (2014) 079, doi:10.1007/JHEP07(2014)079, arXiv:1405.0301.

[15] T. Sjostrand, S. Mrenna, and P. Z. Skands, "A Brief Introduction to PYTHIA 8.1", *Comput. Phys. Commun.* **178** (2008) 852–867, doi:10.1016/j.cpc.2008.01.036, arXiv:0710.3820.

[16] R. Frederix and S. Frixione, "Merging meets matching in MC@NLO", *JHEP* **12** (2012) 061, doi:10.1007/JHEP12(2012)061, arXiv:1209.6215.

[17] CMS Collaboration, "Event generator tunes obtained from underlying event and multiparton scattering measurements", arXiv:1512.00815.

[18] LHC Higgs Cross Section Working Group Collaboration, "Handbook of LHC Higgs Cross Sections: 4. Higgs Properties", technical report.

[19] T. Gleisberg et al., "Event generation with SHERPA 1.1", *JHEP* **02** (2009) 007, doi:10.1088/1126-6708/2009/02/007, arXiv:0811.4622.

[20] GEANT4 Collaboration, "GEANT4: A Simulation toolkit", *Nucl. Instrum. Meth. A* **506** (2003) 250, doi:10.1016/S0168-9002(03)01368-8.

[21] CMS Collaboration, "Particle-Flow Event Reconstruction in CMS and Performance for Jets, Taus, and MET", Technical Report CMS-PAS-PFT-09-001, CERN, 2009. Geneva, Apr, 2009.

[22] M. Cacciari, G. P. Salam, and G. Soyez, "The anti-k_t jet clustering algorithm", *JHEP* **04** (2008) 063, doi:10.1088/1126-6708/2008/04/063.

[23] M. Cacciari, G. P. Salam, and G. Soyez, "FastJet User Manual", *Eur. Phys. J.* **C72** (2012) 1896, doi:10.1140/epjc/s10052-012-1896-2, arXiv:1111.6097.

[24] CMS Collaboration, "Determination of Jet Energy Calibration and Transverse Momentum Resolution in CMS", *JINST* **06** (2011) P11002, doi:10.1088/1748-0221/6/11/P11002.

[25] M. Cacciari and G. P. Salam, "Pileup subtraction using jet areas", *Phys. Lett.* **B659** (2008) 119, doi:10.1016/j.physletb.2007.09.077.

[26] CMS Collaboration, "Measurement of the inclusive W and Z production cross sections in pp collisions at $\sqrt{s} = 7$ TeV with the CMS experiment", *JHEP* **2011** (2011) 1, doi:10.1007/JHEP10(2011)132.

[27] CMS Collaboration, "Electron and Photon performance using data collected by CMS at $\sqrt{s}$ = 13 TeV and 25ns", Technical Report CMS-DP-2015-067, CERN, Dec, 2015.

[28] CMS Collaboration, "Identification of b-quark jets with the CMS experiment", *JINST* **8** (2013) P04013, doi:10.1088/1748-0221/8/04/P04013, arXiv:1211.4462.

[29] D. L. Rainwater, R. Szalapski, and D. Zeppenfeld, "Probing color singlet exchange in Z + two jet events at the CERN LHC", *Phys. Rev.* **D54** (1996) 6680–6689, doi:10.1103/PhysRevD.54.6680, arXiv:hep-ph/9605444.

[30] G. Cowan et al., "Asymptotic formulae for likelihood-based tests of new physics", *Eur. Phys. J. C* **71** (2011) 1, doi:10.1140/epjc/s10052-011-1554-0, arXiv:1007.1727.

[31] P. D. Dauncey, M. Kenzie, N. Wardle, and G. J. Davies, "Handling uncertainties in background shapes: the discrete profiling method", *JINST* **10** (2015), no. 04, P04015, doi:10.1088/1748-0221/10/04/P04015, arXiv:1408.6865.

[32] J. Butterworth et al., "PDF4LHC recommendations for LHC Run II", *J. Phys.* **G43** (2016) 023001, doi:10.1088/0954-3899/43/2/023001, arXiv:1510.03865.

[33] F. Demartin et al., "The impact of PDF and alphas uncertainties on Higgs Production in gluon fusion at hadron colliders", *Phys. Rev.* **D82** (2010) 014002, doi:10.1103/PhysRevD.82.014002, arXiv:1004.0962.

[34] S. Carrazza et al., "An Unbiased Hessian Representation for Monte Carlo PDFs", *Eur. Phys. J.* **C75** (2015), no. 8, 369, doi:10.1140/epjc/s10052-015-3590-7, arXiv:1505.06736.

[35] CMS Collaboration, "First measurement of the differential cross section for $t\bar{t}$ production in the dilepton final state at $\sqrt{s} = 13$ TeV", Technical Report CMS-PAS-TOP-15-010, CERN, 2015. Geneva, Dec, 2015.

[36] LHC Higgs Cross Section Working Group Collaboration, "Handbook of LHC Higgs Cross Sections: 3. Higgs Properties", doi:10.5170/CERN-2013-004, arXiv:1307.1347.

A Additional figures

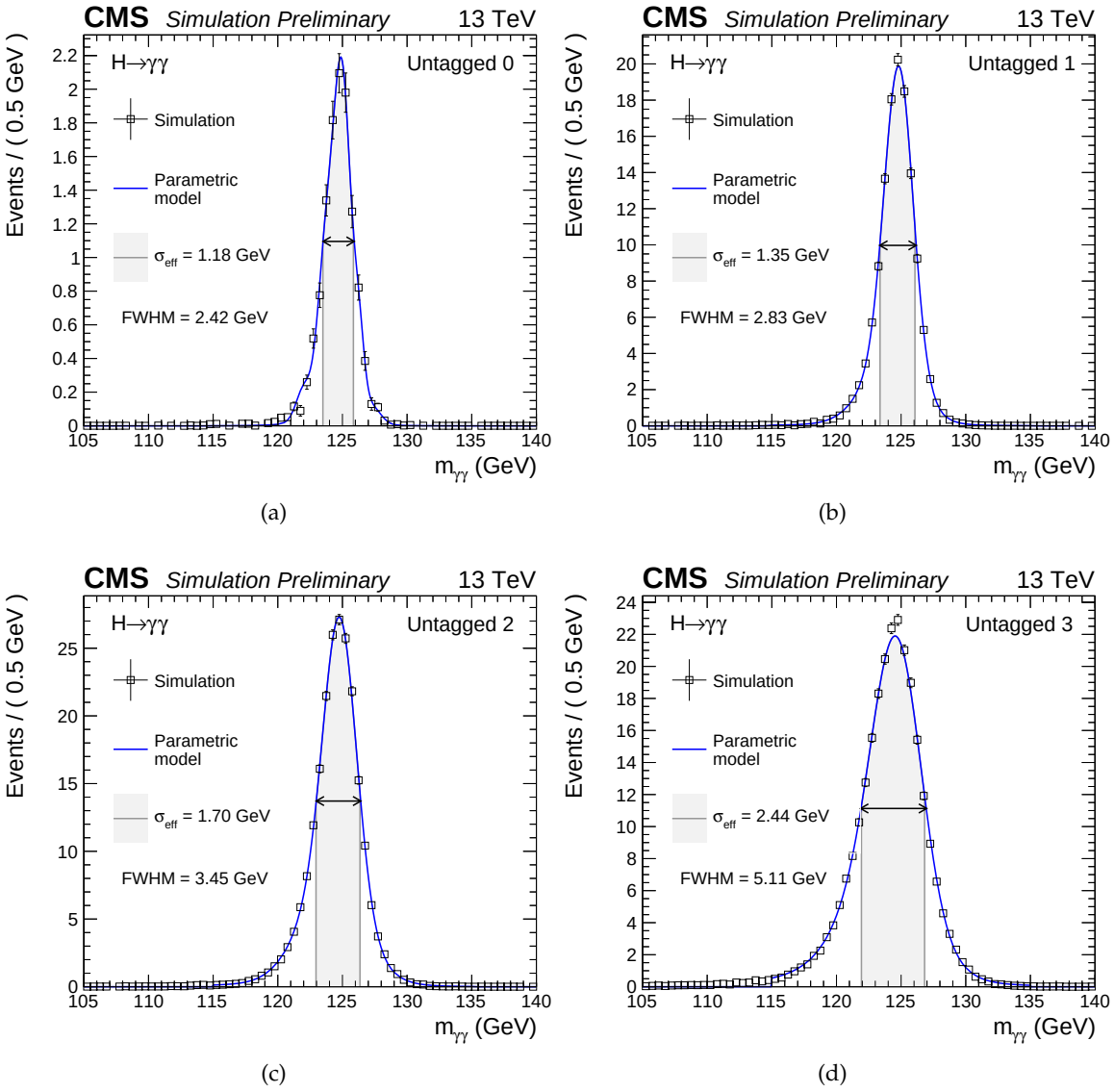

Figure 21: Parametrized signal shapes for the inclusive categories, for a simulated $H \to \gamma\gamma$ signal sample with $m_H = 125$ GeV. The black points represent weighted simulation events and the blue lines are the corresponding models. Also shown are the σ_{eff} value (half the width of the narrowest interval containing 68.3% of the invariant mass distribution), FWHM and the corresponding interval.

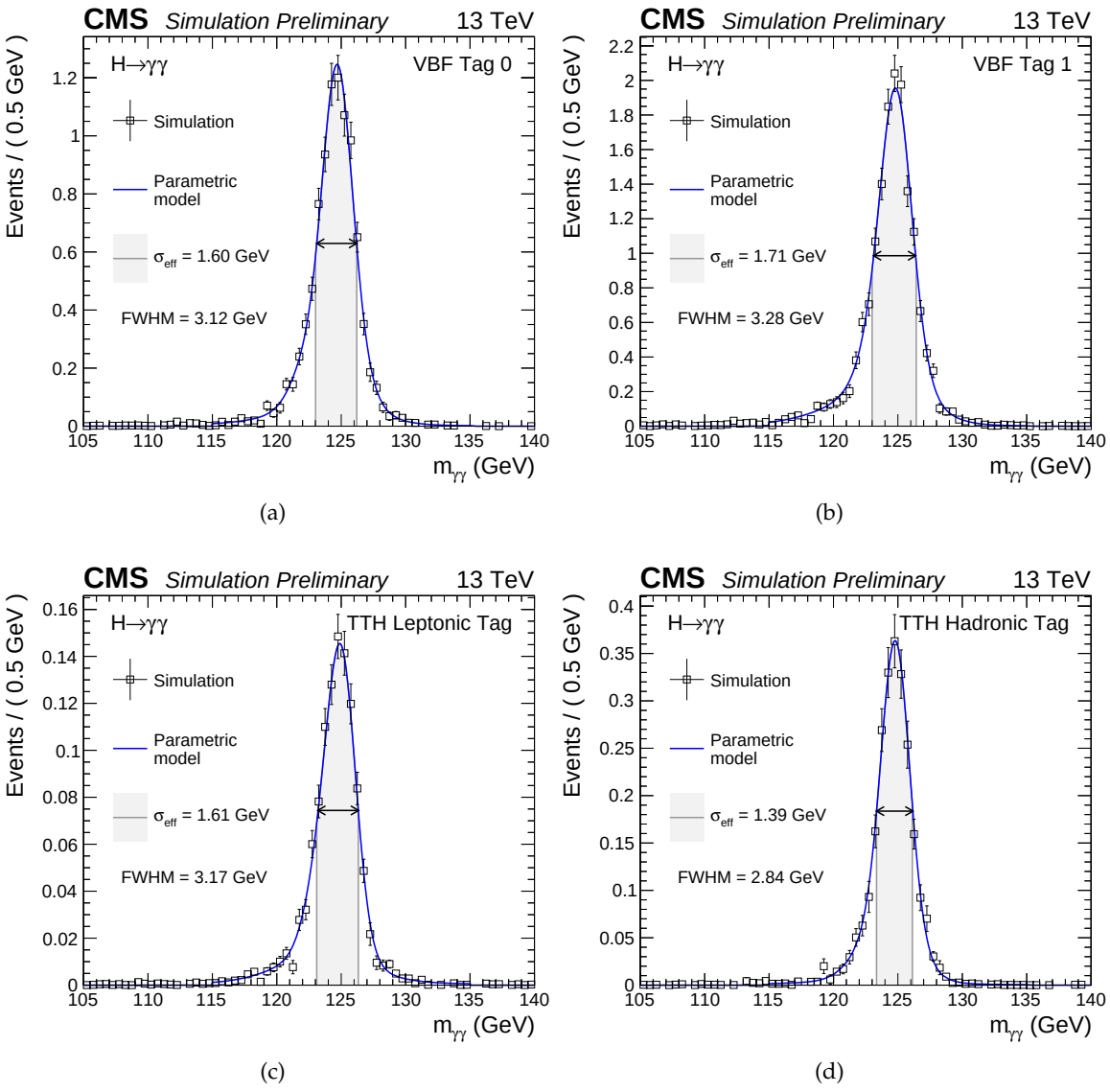

Figure 22: Parametrized signal shapes for the VBF and TTH categories, for a simulated $H \to \gamma\gamma$ signal sample with $m_H = 125$ GeV. The black points represent weighted simulation events and the blue lines are the corresponding models. Also shown are the σ_{eff} value (half the width of the narrowest interval containing 68.3% of the invariant mass distribution), FWHM and the corresponding interval.

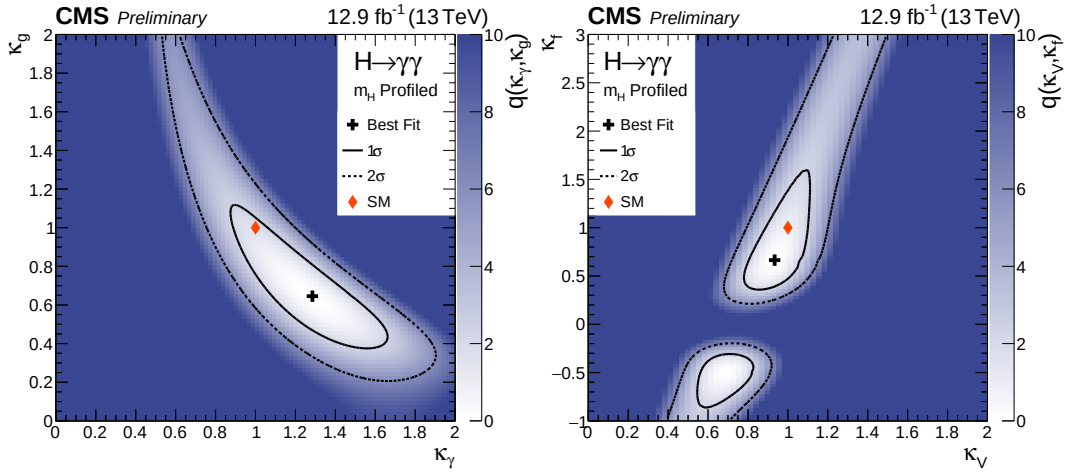

(a) (b)

Figure 23: Two-dimensional likelihood scans of κ_f versus κ_V (a) and κ_g versus κ_γ (b) are shown. The variables κ_V and κ_f are, respectively, the coupling modifiers of the Higgs boson to vector bosons and to fermions while κ_γ and κ_g are the effective coupling modifiers to photons and to gluons [36]. All four variables are expressed relative to the SM expectations. The mass of the Higgs boson is profiled in the fits. For each scan, the value of the Higgs boson mass is profiled The standard model expectation is marked with a red diamond.

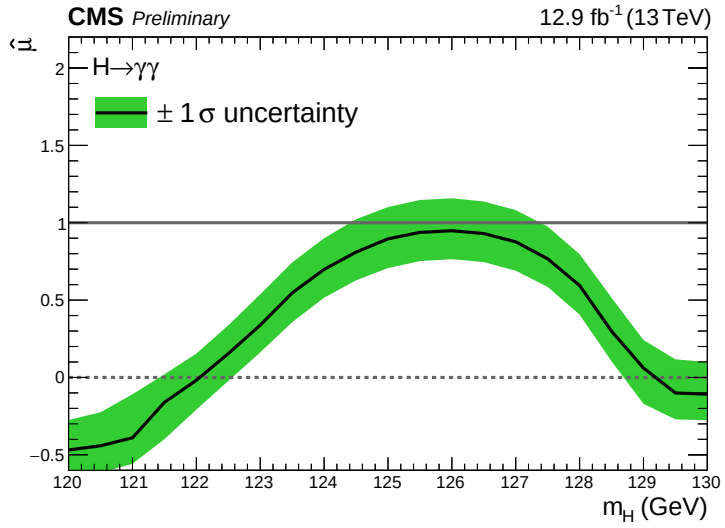

(a)

Figure 24: The figure shows the result of performing a one-dimensional likelihood scan of the signal strength for various values of m_H. The green band represents the uncertainties on the value of the signal strength at each point.

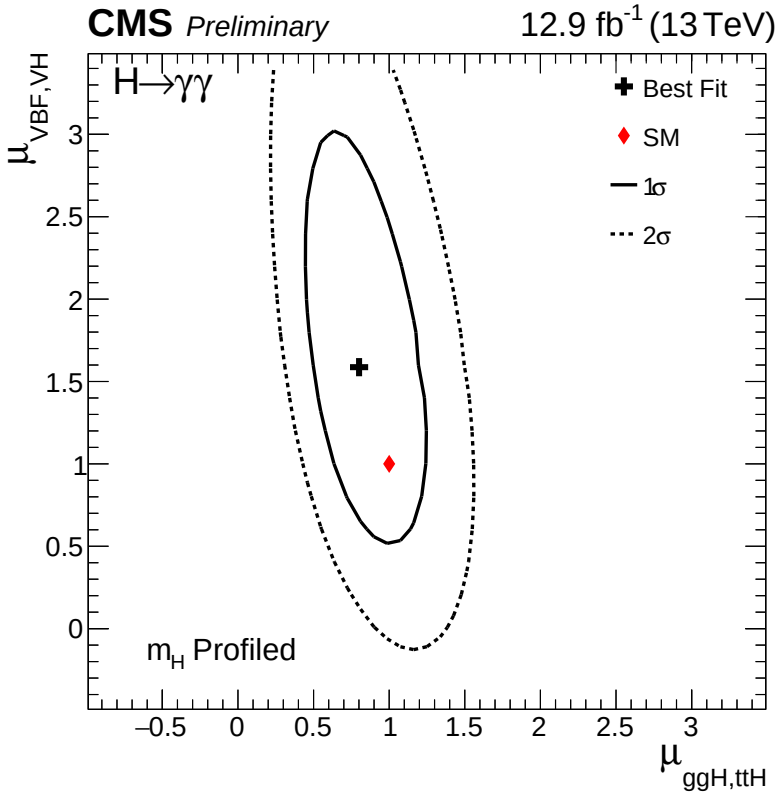

Figure 25: The two-dimensional best-fit (black cross) of the signal strengths for fermionic (ggH, $t\bar{t}H$) and bosonic (VBF, ZH, WH) production modes compared to the SM expectations (red diamond). The Higgs boson mass is profiled in the fit. The solid (dashed) line represents the 1 standard deviation (2 standard deviation) confidence region. The axis ranges have been chosen to be exactly the same as those from the equivalent plot from Run 1 (Fig. 23 in [9]).

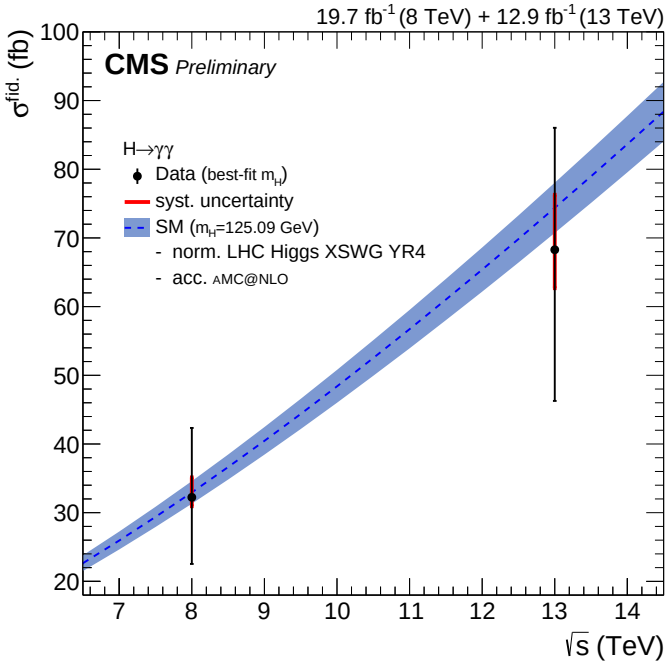

Figure 26: The results of the measurements of the fiducial cross section by CMS at 8 TeV (from the Run 1 analysis [9]) and (13 TeV from this analysis) are shown. The black markers represent the best-fit value of the fiducial cross section for the best-fit mass in each case, along with the corresponding uncertainties. The red lines represent the size of the systematic component on the uncertainty. The blue dashed line and shading represent the SM expected fiducial cross section and uncertainty for a Higgs boson of mass $m_H = 125.09$ GeV. The normalisation has been set using the latest values from [18] and the acceptance is defined using the aMC@NLO generator-level quantities in both cases.